ALL-OPTICAL 3D PHOTOACOUSTIC SCANNER FOR CLINICAL VASCULAR IMAGING

N.T. Huynh*[1,2], E. Zhang*[1,2], O. Francies[4], F. Kuklis[7], T. Allen[1], J. Zhu[1], O. Abeyakoon[4], F. Lucka[5], M. Betcke[3], J. Jaros[6], S. Arridge[3], B. Cox[1], A. Plumb[4], P. Beard[1,2]

[1]Department of Medical Physics and Biomedical Engineering, University College London, UK
[2]Wellcome/EPSRC Centre for Interventional and Surgical Sciences, University College London, UK
[3]Department of Computer Science, University College London, UK
[4]University College London Hospital NHS Foundation Trust, UK
[5]Centrum Wiskunde & Informatica, Amsterdam, The Netherlands
[6]Faculty of Information Technology, Brno University of Technology, Czech Republic

*These authors contributed equally to the work.

Abstract

Visualising superficial vascular anatomy is required for the clinical assessment of diabetes, inflammatory skin diseases, soft tissue damage and other conditions characterised by microvascular pathologies. In principle, photoacoustic tomography (PAT) can meet this need. However, in practice, image quality tends to be limited by the sensitivity and bandwidth limitations of traditional piezoelectric ultrasound detectors commonly used in PAT instruments. PAT scanners based on an all-optical Fabry-Perot ultrasound sensor offer a potential solution. They can provide highly detailed 3D microvascular images but excessively long acquisition times (several minutes) has precluded their clinical application to date. Here, we show that this limitation has been overcome. By variously parallelising the sensor read-out optical architecture, using high PRF excitation lasers and exploiting compressed sensing principles, scan-times have been reduced by up to three orders-of-magnitude enabling 3D image acquisition in a few seconds or even hundreds of ms. By minimising motion-related artefacts, we show this enables acquisition of unprecedentedly detailed 3D images of complex human vascular anatomy revealing individual capillaries, arterioles, venules, venous valves and mm-scale arteries and veins to depths approaching 15 mm. In addition, we show that it permits dynamic 3D imaging enabling the visualisation of haemodynamic events such as time-varying tissue perfusion. These developments unlock the clinical potential of the technology. To demonstrate this, exploratory case studies on patients were conducted showing that the scanner can visualise and quantify microvascular changes associated with peripheral vascular disease, skin inflammation and rheumatoid arthritis. These attributes suggest the technology could find broad application across a range of clinical specialities amongst them cardiovascular medicine, oncology, dermatology and rheumatology.

INTRODUCTION

Visualising the microvasculature to sub-cm depths in tissue is required for the effective clinical management of a wide range vascular abnormalities, including those associated with skin cancers[1], dermatological conditions[1], the diabetic foot[2] and superficial soft tissue damage such as burns or ulcers[3]. Optical imaging techniques offer promise on account of their ability to visualise vascular anatomy, oxygenation and flow[4,5]. However, strong optical scattering by tissue limits penetration depth or spatial resolution. Conventional light microscopy, optical coherence tomography and other methods that rely on un-scattered ballistic photons can provide capillary-level microvascular images but only to sub-mm depths. Laser Doppler or speckle contrast imaging that exploit diffuse or semi-ballistic photons provide greater penetration depth. However, optical scattering limits spatial resolution resulting in spatially averaged images that do not reveal microvascular architecture at the level of individual arterioles and venules. Ultrasound (US) imaging can overcome the depth/resolution limitations of optical techniques but presents other challenges. Conventional non-contrast clinical Doppler US yields poor microvascular contrast with emerging ultrafast plane-wave US[6,7] offering higher sensitivity. However, both rely on the detection of moving blood thus limiting sensitivity to slowly moving or static blood and precluding the measurement of blood oxygenation.

Photoacoustic imaging provides an alternative that can address the limitations of conventional optical and ultrasound imaging[8,9,10,11,12]. In its most common implementation, referred to herein as widefield photoacoustic tomography (PAT)[8], a large area pulsed laser beam flood-illuminates the tissue. Optical absorption by haemoglobin produces impulsive heating and the subsequent generation of broadband ultrasound waves. By detecting these waves at the skin surface, an image of the vasculature can be reconstructed. Since ultrasound waves are scattered in tissue much less than photons, PAT avoids the range-resolution limitations that afflict optical methods: cm-scale penetration depths with depth-dependent spatial resolution ranging from tens to hundreds of micrometres are achievable. Moreover, unlike US, PAT directly detects haemoglobin rather than relying on blood flow as a surrogate vascular marker. It therefore offers the prospect of visualising small vessels characterised by low blood flow otherwise indistinguishable with US as well as the spectroscopic measurement of blood oxygenation[13]. These attributes have led to PAT being investigated for the clinical assessment of microvascular changes associated with cancer[14,15], cardiovascular disease[16,17], diabetes[18], inflammatory conditions[19,20,21,22] and soft tissue damage[23,24].

Despite its promise, the practical implementation of PAT presents significant instrumentation related challenges. These become particularly acute when imaging superficial vascular anatomy to sub-cm depths. For such shallow depths, frequency-dependent acoustic attenuation is modest resulting in broadband photoacoustic signals with a frequency content that extends to several tens of MHz. Accurately recording the photoacoustic wavefield thus requires a commensurately wide detection bandwidth, fine spatial sampling on a tens of micron scale to satisfy spatial Nyquist and sub-100µm element sizes. A transparent detector is also desirable to permit delivery of the excitation laser beam through the detector. Traditional piezoelectric ultrasound detectors are most commonly used in PAT scanners but tend to be insufficiently broad-banded, offer poor sensitivity for sub-100µm element sizes and are optically opaque. Moreover, for clinically acceptable 3D frame rates, a 2D detector array composed of $>10^4$ micron-scale elements would be required but is unachievable with conventional ultrasound detection technology. Acoustic-resolution photoacoustic microscopy (AR-PAM)[25,26] is an alternative high resolution photoacoustic imaging mode. However it relies on mechanically scanning a focused detector resulting in long acquisition times (typically > 1 minute) and the fixed focal depth of the detector limits the penetration depth range.

Ultrasound detectors based on optically resonant structures have the potential to overcome the limitations of piezoelectric receivers on account of their wide bandwidth, small element size, high sensitivity and optical transparency[27,28,29,30,31,32,33,34,35,36]. However, few have made the transition from the laboratory to practical *in vivo* PAT imaging tool. One exception is the Fabry Perot (FP) polymer film ultrasound sensor[36] which has been used in a range of 3D PAT scanners, mostly for imaging mice. It has been shown that these systems can provide *in vivo* 3D PAT vascular images[37,38,39,40,41,42,43] to sub-cm depths with superior image quality to conventional piezoelectric based PAT scanners. However,

the clinical translation of the technology has been hindered by slow acquisition speed, a consequence of the sequential nature of the FP sensor read-out scheme and the large number of detection points (>10^4) required to reconstruct a 3D image. These factors conspire to produce scan-times of the order of minutes. Although acceptable for imaging relatively immobile targets such as anaesthetised mice, routine clinical use on humans requires acquisition on a scale of seconds or hundreds of milliseconds to minimise motion-related artefacts and align with clinical workflows.

In the current work, we demonstrate a practical FP based scanner that can meet the clinical need for fast acquisition by overcoming the slow speed of early generation systems. By exploiting a novel parallelised sensor readout scheme, high PRF excitation lasers and compressed sensing techniques, up to three orders-of-magnitude faster acquisition has been achieved. We show that scan-times of a few seconds or even a few hundred ms are now possible enabling high fidelity 3D images without motion-artefacts to be acquired repeatably in humans. In addition, dynamic 3D imaging is now possible allowing real-time probe placement and visualisation of dynamic physiological events. The acceleration in acquisition speed that has been achieved unlocks the clinical potential of the technology for the first time. We illustrate this by evaluating the scanner on volunteers and hospital patients and showing that it can provide detailed 3D vascular images at a variety of anatomical locations and visualise disease-specific microvascular changes associated with diabetes, skin inflammation and rheumatoid arthritis. These demonstrations illustrate the potential of the technology as a tool for the clinical assessment of diseases associated with superficial vascular pathologies.

RESULTS

Fabry Perot planar PAT scanner: system overview and characteristics

The custom-built scanner is shown in Figure 1. It comprises an optical parametric oscillator (OPO) excitation laser system for generating the photoacoustic waves and a Fabry-Perot (FP) ultrasound scanner for mapping them over the surface of the skin. Fig 1(a) illustrates its working principles. Nanosecond laser pulses in the 700-900nm spectral range where tissue attenuation is low are emitted by the OPO and coupled into a delivery optical fibre. The light emerges from the distal end of the fibre producing a large diameter (>20 mm) beam incident on the FP ultrasound sensor head, the acoustically-sensitive element of which is a thin film polymer Fabry Perot interferometer (FPI). Since the FPI is transparent in the 560nm – 1300nm wavelength range (Suppl. Figure 1), the excitation beam passes through the sensor and flood-illuminates the underlying tissue thereby generating broadband ultrasound waves. These waves propagate to the FPI, where they modulate its optical thickness and thus its reflectivity. The latter is then read-out by sequentially scanning an array of up to 64 focused laser beams over the surface of the sensor step-by-step; one step per excitation laser pulse. In this way, the spatial-temporal distribution of the incident photoacoustic wavefield can be mapped in 2D enabling a 3D image to be reconstructed.

The maximum rectangular scan area that the scanner can provide is 21 x 19.5 mm^2. For the step sizes of dx=dy=108 µm and dx=dy=54 µm used in this study, this enables the synthesis of arrays of 34,560 and 138,240 detection points respectively. Dense spatial sampling on this scale is a pre-requisite for short-range high resolution PAT and achievable with the FP sensor by virtue of the optical nature of its read-out scheme but unattainable with current conventional ultrasound detection technology. As shown in Figure 1c, the sensor also provides the necessarily wide frequency response (50kHz – 35 MHz) to capture the broadband frequency content of photoacoustic signals generated in tissue, a requirement that is also challenging to meet using conventional methods. The combination of dense spatial sampling and widebandwidth that the system provides yields near acoustic-diffraction limited spatial resolution (see Methods); at the centre of the scan area, the lateral resolution varies from 60µm to approximately 120µm over the depth range 1mm to 12mm (Figure 1d).

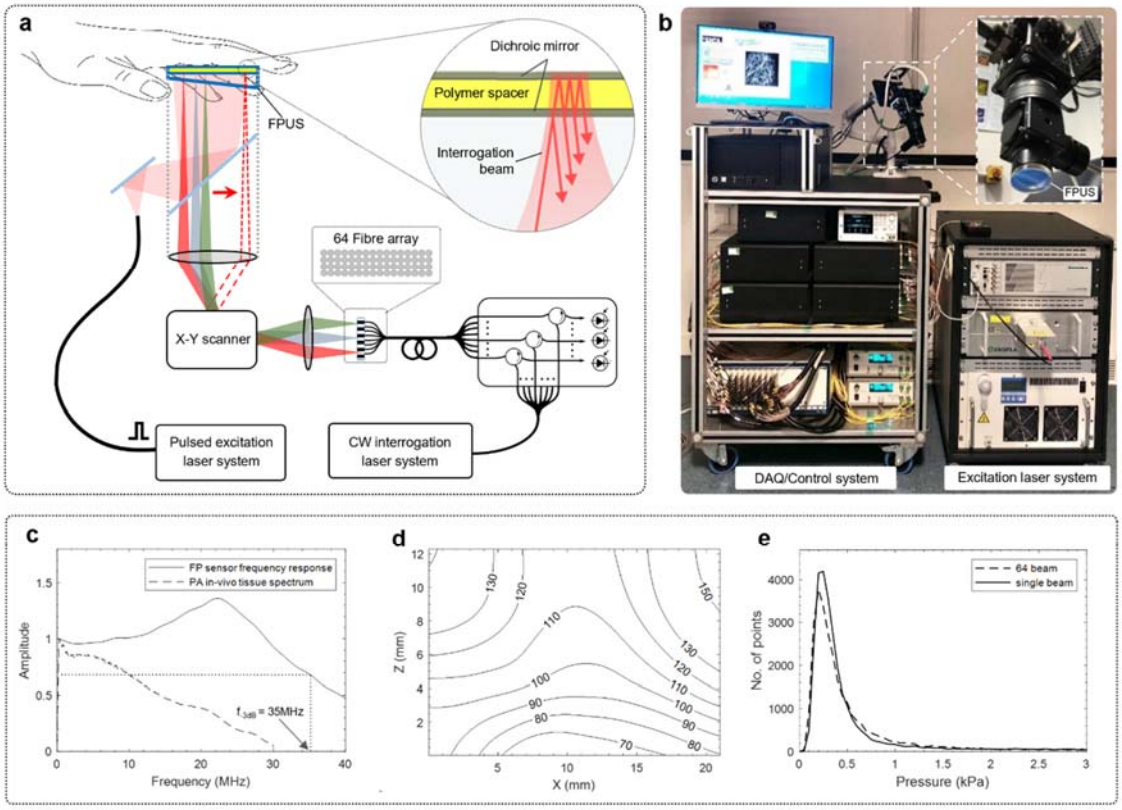

Figure 1 Multibeam Fabry Perot (FP) based photoacoustic tomography (PAT) scanner. (a) Schematic showing scanner read-out architecture and FP ultrasound sensor (FPUS) structure. (b) Photograph of scanner showing cart-based acquisition system, imaging head (inset) and OPO excitation laser system. (c) Frequency response of FP sensor with 24.6µm FPI spacer (f_{-3dB}=35MHz) and acoustic frequency spectrum of photoacoustic signals generated *in vivo* in human palm (see Methods), (d) Lateral spatial resolution in microns for scan step size dx=dy=108 µm. (e) Noise-equivalent-pressure (NEP) distribution for 64 beam and single beam scanners over 21 x 19.5 mm^2 scan area (see Methods).

The measured vertical resolution depends largely on the sensor bandwidth and was found to be spatially invariant at 45µm over the FOV. The FP sensor also offers high sensitivity with small element size. Figure 1e shows a histogram of the noise equivalent pressure (NEP) distribution over a scan area of 21 x 19.5 mm^2. The modal NEP is 0.2 kPa (over a 20MHz measurement bandwidth) and achieved using an interrogation beam spot diameter (1/e^2) diameter of ~49µm which, to a first approximation, corresponds to the acoustic element size[44]. By comparison, the sensitivity of an equivalent sized broadband PVDF piezoelectric receiver would be more than two orders of magnitude lower, due to the scaling between piezoelectric sensitivity and element area[31].

Accelerated acquisition implementation

The key technical advance that has been made relates to accelerating the acquisition speed. To achieve this, two strategies were variously employed. The first involved increasing the A-line acquisition rate by parallelising the sensor read-out and using high PRF excitation lasers. In the second, a compressed sensing approach was adopted permitting sub-sampling of the acoustic detection aperture and thus a reduction in the total number of A-lines required to form an image.

The parallelisation of the FP sensor read-out was achieved using a multibeam scanner which scans an array of N interrogation beams across the sensor; N=16 or N=64, with the latter most commonly used and assumed in the following description. As shown in figure 1a, the output of the interrogation laser system (see Methods) is divided into 64 single mode 9µm core fibres using a passive fibre splitter. Each fibre is connected to a fibre circulator and recombined to form a fibre bundle comprising four rows of sixteen fibres with a core-to-core separation of 80µm. The divergent output of each fibre in the bundle is incident on a lens that collimates all 64 beams and brings them together

to form a pivot point on the input of a 2-axis conjugate galvanometer based scanner. The output of the scanner is focused on to the FP sensor plane, resulting in an array of 64 focused spots each separated by 324μm. The 64 beams are reflected from the sensor, back through the scanner, re-coupled into their respective single mode fibres and delivered via circulators to individual InGaAs photodiode-transimpedance amplifier units each connected to a 64 channel RF digitiser. By scanning the array of 64 beams across the sensor surface and recording the acoustically-induced time-varying reflected optical power modulation simultaneously on all 64 channels at each scan point, a map of the incident photoacoustic field can be recorded. In all cases in this study, single-shot acquisition without signal averaging was used.

Parallelising the detection in this way sets a specific technical challenge. In order to detect a signal, it is necessary to tune the interrogation laser to a wavelength that aligns with the edge of the FPI cavity resonance, denoted the optimum bias wavelength λ_b[36]. Since the interrogation laser wavelength is identical for all 64 beams, the FPI polymer spacer thickness must be sufficiently uniform that λ_b is spatially invariant to within ~0.1nm over the rectangular area dA_b on the sensor occupied by the 64 focused beams. For a typical spacer thickness of 25μm, this requires a thickness uniformity less than 1.6 nm over dA_b, a non trivial requirement for polymeric films. If this condition is not met, the acoustic sensitivity will vary from one beam to the next, compromising the reconstructed image SNR. Spacer thickness uniformities as low as 3nm over 1cm^2 were achieved corresponding to ~ $\lambda/500$; for comparison, the thickness uniformity of a high quality solid fused silica etalon rarely exceeds $\lambda/100$. This level of thickness uniformity comfortably surpasses the requirement for λ_b parity over dA_b as evidenced by figure 1e, which shows that the spatial distribution of the NEP of a 64 beam scanner is comparable to that of a single beam scanner.

Fast acquisition was further enabled by using excitation lasers operating at high PRFs and optimising the scanner control and data acquisition hardware to accommodate these PRFs. Frequency doubled Nd:YAG pumped Type 2 Optical Parametric Oscillator (OPO) laser systems, emitting 5ns pulses at PRFs up to 200 Hz were used for most imaging studies (see Methods). In addition a custom Yb fibre laser[51] operating at a PRF of 1kHz emitting 20 ns pulses was used to approach the maximum achievable A-line rate limited by the system hardware. The combination of parallelising the sensor read-out and operating at these relatively high PRFs, enabled significant A-line rate acceleration. Depending on N and the PRF, A-line rates between 1,400 and 64,000 A-line/s were achieved, compared to the 50 A-Lines/s of early generation single-beam pre-clinical FP scanners[42]. Reducing the scan-time by sub-sampling the scan area to reduce the total number of scan points was also evaluated. By exploiting the data redundancy in the photoacoustic wavefield within a compressed sensing framework[45] (see Methods), sub-sampling factors of 50%, 25% and 12.5% were used with corresponding reductions in scan-time.

The above methods have reduced the time required to acquire a 3D image data sets; depending on the imaging parameters used, scan-times on a scale of seconds to hundreds of ms were achieved.

3D *in vivo* vascular imaging

To demonstrate the rapid, volumetric imaging capabilities of the scanner, images of vascular anatomy and haemodynamic events were acquired using healthy adult volunteers as research participants (see Methods). To acquire an image, the probe head was positioned at the anatomical region of interest, a bolus of ultrasound gel inserted between the FP sensor and the skin to provide acoustic coupling and the scan sequence commenced.

Figure 2 shows maximum intensity projections (MIP) of 3D image data sets acquired at different positions on the hand and wrist. These images were reconstructed in <1s using a k-space method[46] from 34,560 photoacoustic A-lines recorded over a scan area of 21 x 19.5 mm^2 in 108µm steps. The PRF-limited A-line rate was 6,400 A-lines/s resulting in a total scan time T=5.4s. By contrast, early generation single-beam FP scanners[36] would have required T>5 minutes to perform an identical scan.

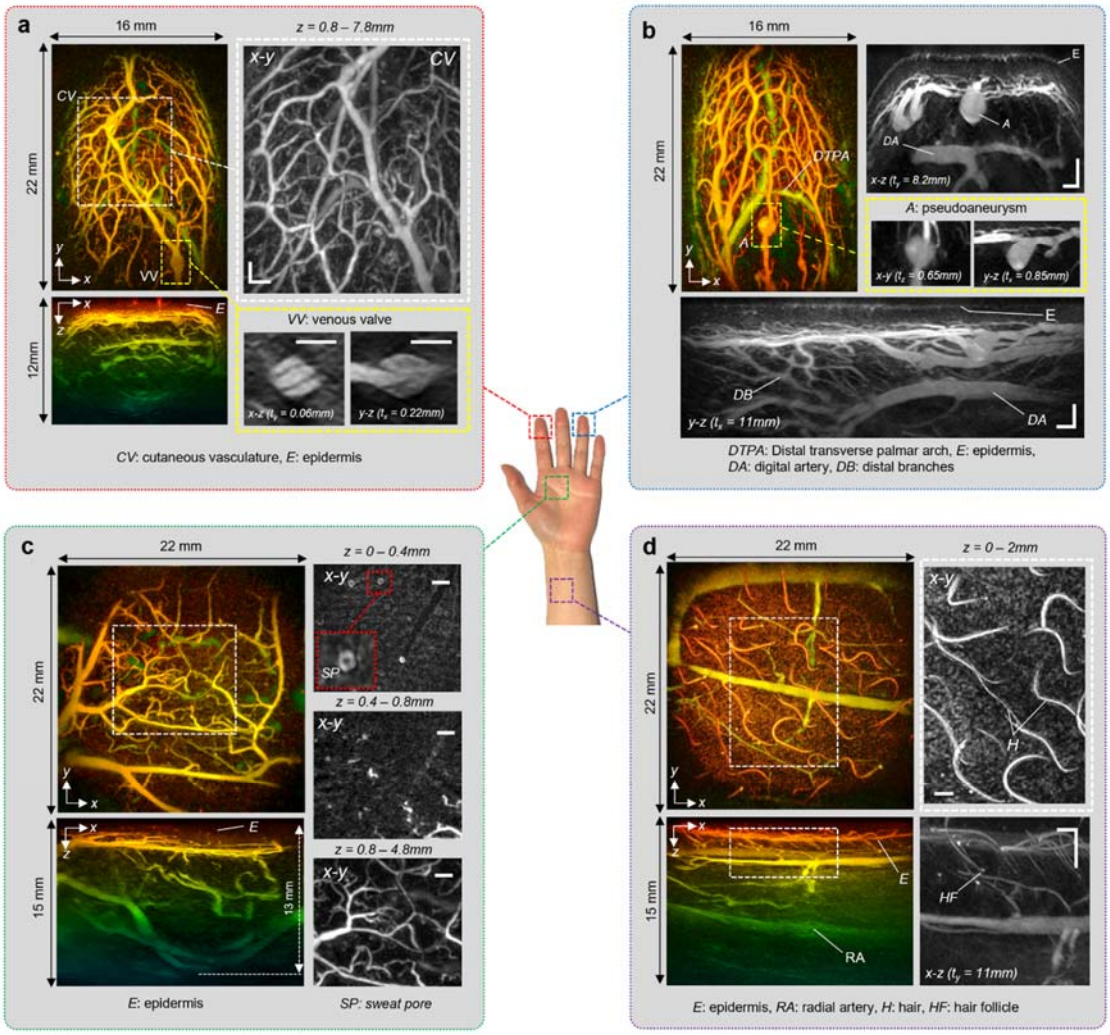

Figure 2 PAT images of the hand and wrist regions; (a) Index finger-tip. *Left*; x-y and x-z depth-to-colour encoded MIPs. *Right,* expanded view greyscale MIPs showing en-face view of cutaneous vasculature (CV) anatomy and cross-sectional views of a venous valve (VV). (b) Ring finger-tip. *Left;* x-y depth-to-colour encoded MIP. *Right;* expanded view greyscale MIPs showing cross-sectional view of dermal microvascular anatomy, epidermis (E), digital artery (DA) and pseudoaneurysm (A) and *Lower;* expanded view y-z greyscale cross-sectional MIP showing distal branches (DB) and digital artery (DA). (c) Palm region. x-y and x-z depth-to-colour encoded MIPs showing vascular anatomy to a depth of 13mm. *Right;* expanded view x-y en-face greyscale MIPs for three different depth ranges for region indicated by white dotted box. (d) Wrist region. x-y and x-z colour-depth encoded MIPs, the latter showing the radial artery (RA). *Right* expanded view greyscale MIPs of region indicated by white dotted box showing hair (H) and hair follicles (HF). Scale bars: 1mm. t_x and t_y: slice thicknesses of y-z and x-z greyscale MIPs respectively. Imaging parameters: λ=850nm, dx=dy=108µm, dt=16.67ns, PRF=100Hz, N=64, A-line rate: 6400 A lines/s, scan-time: T=5.4s.

As figure 2 shows, the scanner provides detailed volumetric images of the microvasculature to depths approaching 15 mm. The images of the index and ring finger-tips (figures 2a and 2b) show a superficial layer (E) less than 200µm thick. This is the predominantly avascular epidermis with the contrast provided by melanin rather than haemoglobin absorption - see Suppl. Figure 2 for additional depth-resolved visualisations. Beneath the epidermis, at a depth of approximately 0.5mm, dense networks of small vessels within the superficial papillary plexus are visible. In this region, individual vessels with reconstructed lateral and vertical dimensions down to 80µm and 50µm respectively are visible. At greater depths, the larger vessels in the reticular plexus, the distal transverse palmar arch (DTPA) and the digital artery (DA) in the hypodermis can be seen (figure 2b). Other structures include venous microvalves (VV) in the superficial papillary plexus, most evidently in the lower right x-z and y-z greyscale images in figure 2a. These images reveal the V-shaped structure characteristic of the internal folds that serve as the leaflets of a bicuspid venous valve, also observed in TEM images of resin casts of valves[47] but not previously visualised *in vivo* in 3D in sub-mm venules. Another distinctive vascular structure is the berry shaped feature protruding from a superficial vessel as shown in figure 2(b), possibly a pseudoaneurysm (A) or saccular dilation. The image of the palm and wrist regions (Figures 2c and 2d) show a thicker epidermis, a less dense superficial vasculature, large vessels such as the radial artery (figure 2d) and greater penetration depth with discernible vascular anatomy at a depth of 13mm (figure 2c). Also visible are non-vascular structures including sweat pores, skin sulci, hair and hair follicles.

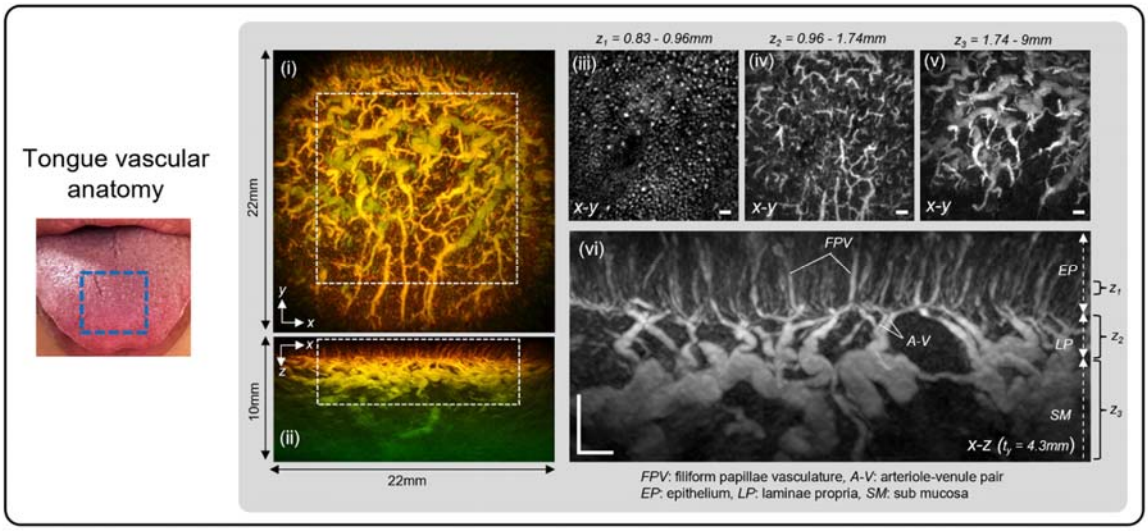

Figure 3: PAT image of the tongue dorsum. (i) x-y and (ii) x-z depth-to-colour encoded MIPs. Greyscale x-y MIPs of region indicated by dotted white rectangle in (i) for (iii) 0.13mm thick slice through the epithelium (EP), z=0.83mm to 0.96mm. (iv) 0.78mm thick slice corresponding to laminae propria (LP), z=0.96 to 1.74mm. (v) 7.26mm thick slice through submucosa (SM) and muscle, z=1.742mmm to 9mm. (vi) Expanded view greyscale x-z MIP of region indicated by white dotted rectangle in (ii) showing filiform papillae (FP) capillary loops, arteriole-venule pair (A-V) and supplying vasculature. Scale bars: 1mm. t_y: slice thicknesses of x-z greyscale MIP. Imaging parameters: λ=875nm, dx=dy=108µm, dt=16.67ns, PRF=100Hz, N=64, A-line rate: 6400 A lines/s, scan-time: T=5.4s.

To demonstrate the versatility of the scanner, other regions of the body that exhibit different distinctive vascular anatomy were scanned. Figure 3 shows an image of the dorsal region of the tongue illustrating the rich diversity of vascular architectures, orientations and length scales that can be visualised. The superficially located near-vertical capillaries in the filiform papillae and their supplying arteriole-venule pairs, the dense network of microvessels in the lamina propria and the larger mm-scale horizontally-aligned supplying vessels in the underlying sub-mucosa and muscle are all visible.

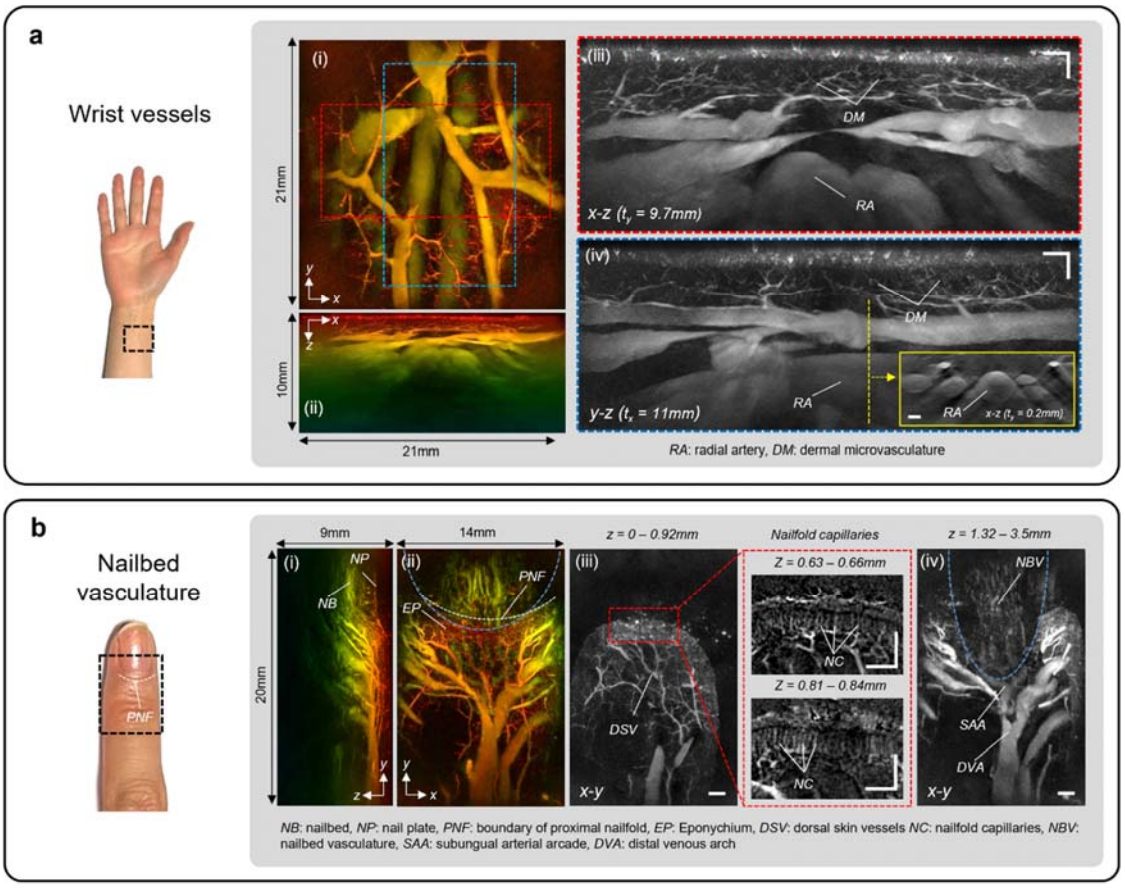

Figure 4: PAT images of the wrist and nailbed vasculature acquired in high resolution scan mode. (a) Wrist region, (i) x-y and (ii) x-z depth-to-colour encoded MIPs, (iii) x-z and (iv) y-z greyscale MIP slices of regions indicated by dotted red and blue rectangles in (i) showing fine dermal microvasculature (DM), radial artery (RA) and large wrist veins. Inset*:* x-z greyscale MIP showing cross-sectional view of the radial artery and adjacent veins in the plane indicated by the white dotted line in (iv). (b) Nailfold and nailbed region of the finger, (i) y-z depth-to-colour encoded MIP showing dermal vasculature, nail plate (NP) and nailbed (NB). (ii) x-y depth-to-colour encoded MIP showing en-face view of supplying vascular tree and eponychium (EP). White dotted line represents the boundary of the proximal nailfold (PNF). (iii) x-y MIP greyscale slice (z=0 – 0.92mm*)* revealing dorsal skin vessels (DSV) and nailfold capillary (NC) region. *Right:* expanded view of red dotted rectangle showing layers of nailfold capillaries at two different depths. (iv) x-y MIP greyscale slice (z=1.32 - 3.5mm) showing nailbed vasculature, subungual arterial arcade (SAA) and distal venous arch (DVA). In (ii) and (iv), the region visualised within the blue dotted line lies beneath the nailplate. To account for the higher speed of sound in the nail, this region was reconstructed using a different sound speed (c=1650 m/s) to the surrounding region (c=1547 m/s) enabling improved visualisation of the vasculature beneath the nailplate. Scale bars: 1mm. t_x and t_y*:* slice thicknesses of y-z and x-z greyscale MIPs respectively. Imaging parameters: λ=850nm, dx=dy=50µm, dt=16.67ns, PRF=100Hz, N=64, A-line rate=6400 A lines/s, scan-time T=29s.

To acquire even more detailed images, a high resolution scan mode in which the step size was reduced to 54µm was used. Figure 4 shows an image of the vessels in the wrist acquired in this mode. At depths below 2mm, the fine dermal microvasculature (DM) can be seen. In this region, individual vessels with reconstructed lateral and vertical dimensions down to 45µm and 35µm respectively are visible. In addition, much larger mm-scale vessels such as the radial artery can be seen. It is notable that the interiors, as well as the edges, of these vessels are clearly visualised, most apparently in the inset x-z MIP in Figure 4a(iv). This is a consequence of the broad bandwidth of the FP sensor which extends down to 50kHz enabling detection of the low acoustic frequencies required to accurately reconstruct mm-scale features. By contrast, images acquired by piezoelectric based PAT scanners tend to visualise only the boundaries of large vessels[48], a consequence of the poor sensitivity at low frequencies of the relatively narrowband piezoelectric receivers used in these systems. A similar high resolution scan was performed on the upper side of the finger in the nailbed area further illustrating the diversity of vascular anatomy that can be visualised. The major digital vessels such as the distal venous arch (DVA) and those constituting the subungual arterial arcade (SAA) can be seen. In addition,

small microvessels, including the nailfold capillaries which can serve as markers of conditions such as rheumatoid arthritis[49] or Reynaulds phenomenon[50] are visible.

These results show that the scanner can provide detailed 3D vascular images of comparable, if not better, quality than previous FP scanners but with acquisition times of the order of seconds rather than minutes.

Accelerated acquisition modes

The detailed nature of the images shown in figures 2-4 suggests that acquisition speed is sufficiently fast to avoid appreciable motion-related image artefacts. However, even faster acquisition is desirable in some circumstances, for example for visualising haemodynamic events. To achieve this, images were acquired using excitation lasers operating at higher PRFs than typically used in PAT and exploiting compressed sensing principles. Figure 5a shows images of a 14 x 14mm^2 region on approximately the same region of the palm at three different PRFs. The images acquired at 100Hz and 200Hz PRFs were obtained at 875nm using an OPO laser system resulting in PRF-limited A-line rates of 6,400 A-lines/s and 12,800 A-line/s and corresponding acquisition times of 3.2s and 1.6s respectively. There is a modest reduction in image SNR at 200Hz due to the lower pulse energy used in order to remain below the maximum permissible exposure (MPE) for skin. To demonstrate that the scanner hardware can operate at even higher PRFs, an image was obtained using a PRF of 1kHz provided by a custom-designed, large core Yb fibre laser[51] (see Methods) emitting at 1064nm. The A-line rate achieved at this PRF was 64,000 A-lines/s, resulting in a scan-time of T=0.3s. Image quality appears not be excessively compromised, given the non-optimal excitation wavelength and low pulse energy of the laser which resulted in a fluence more than one order of magnitude lower than the MPE.

There is inevitably a limit to the scan speed that can be achieved by increasing the PRF to increase the A-line rate. This is dictated by the response time of the galvanometer scanners, data acquisition sampling and transfer rates, the availability of high PRF mJ-scale ns pulsed lasers and, perhaps most importantly, the average power constraints defined by the maximum permissible laser exposure for the skin. The use of spatially sub-sampled data within a compressed sensing framework provides an opportunity to circumvent these limitations. It is based on the notion that the spatial complexity of photoacoustic images is modest and thus conventionally uniformly sampled photoacoustic data contains an element of redundancy. This redundancy can be exploited to reconstruct an image without excessively compromising image SNR by randomly sub-sampling the scan area and employing an iterative model-based variational image reconstruction approach which imposes a sparsity constraint[45]. Since this image is formed from fewer measurements, the scan-time T is reduced accordingly.

The results of using this approach (see Methods) are illustrated in Figure 5b which shows images reconstructed using different sub-sampling factors. These images were obtained by randomly scanning the interrogation beam array in a non-overlapping fashion to acquire a fully sampled (100%) photoacoustic time-series data set with a scan time T=5.4s and image SNR=33dB. Thereafter, sub-sampled data sets were obtained by extracting the first 12.5%, 25% and 50% of the recorded data from the 100% data set with corresponding scan times of T=0.7s, T=1.35s and T=2.7s and image SNRs of 25 dB, 29 dB and 32 dB. As figure 5b shows, SNR and image fidelity scale inversely with sub-sampling factor, although, even when using just 12.5% of the fully sampled data, the main features of the tissue vasculature remain visible. However, the reductions in scan-time are at the cost of increased reconstruction time due to the need to run the forward acoustic propagation model multiple times within the iterative reconstruction scheme used; for example the reconstruction time was >1 hour for the images in Figure 5 compared to <1s for the images in Figure 2. However, recent developments in using deep learning for iterative PAT image reconstruction[52,53] may provide opportunities to reduce computation time.

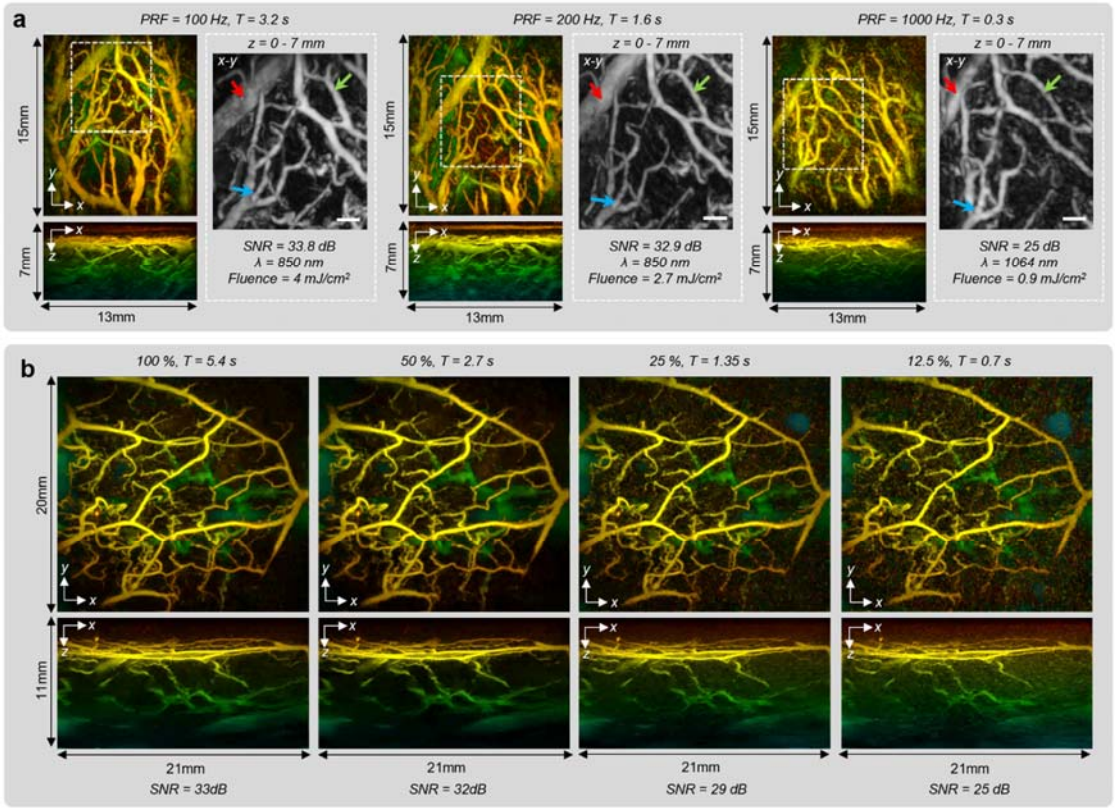

Figure 5: Accelerated PAT acquisition modes: (a) Images of the vasculature acquired at PRFs of 100 Hz, 200 Hz and 1000 Hz. The corresponding A-line rates were 6,400, 12,800 and 64,000 A-lines/s resulting in scan-times of T=3.2s, T=1.6s and T=0.3s respectively. The white dotted rectangle represents the region of the vasculature common to all three images; it is within this region that the SNR is estimated. The greyscale x-y MIPs show expanded views of this region with the red and blue arrows depicting common blood vessels. (b) Images acquired at λ=850nm using fully sampled data (100%) and spatially sub-sampled data with sub-sampling factors of 50%, 25% and 12.5% and corresponding scan times of T=5.4s, T=2.7s, T=1.35s and T=0.7s respectively. A-line rate=6400 A-lines/s. Scale bars: 1mm. Imaging parameters: dx=dy, dx=dy=108µm, dt=16.67ns, N=64.

2D dynamic imaging

The system can provide a 2D video-rate imaging mode for visualising dynamic physiological events or to rapidly search for a region of anatomical interest in real-time prior to switching to the 3D imaging mode. To acquire a 2D image, the 4 x 16 interrogation beam array is scanned along a line on the FP sensor, with the long axis of the array aligned along the scan line. The photoacoustic signals acquired can thus be regarded as equivalent to those acquired from a 1.5D ultrasound array composed of 4 x 16 x m elements, where m is the number of scan steps along the line scan. By performing depth-dependent synthetic receive focussing in the elevation plane of this notional 1.5D array, out-of-plane photoacoustic signals are rejected and the image slice thickness minimised (Figure 6a(i)). To demonstrate the video rate 2D imaging capability of the system, the probe was place on the wrist of a volunteer and translated over the skin surface whilst acquiring images as shown in Video 1. Figure 6a(ii) shows a sequence of 5 frames extracted from this Video corresponding to different probe positions. Several blood vessels and their change in relative lateral position as the probe is moved from right to left can be seen. To acquire these images, the interrogation beam array was scanned along a 15.55 mm long line in steps of 162µm and an excitation laser PRF of 200Hz was used. Hence, the A-line rate was 12,800 lines/s resulting in a single frame scan-time of 30ms and thus a frame rate of 33fps.

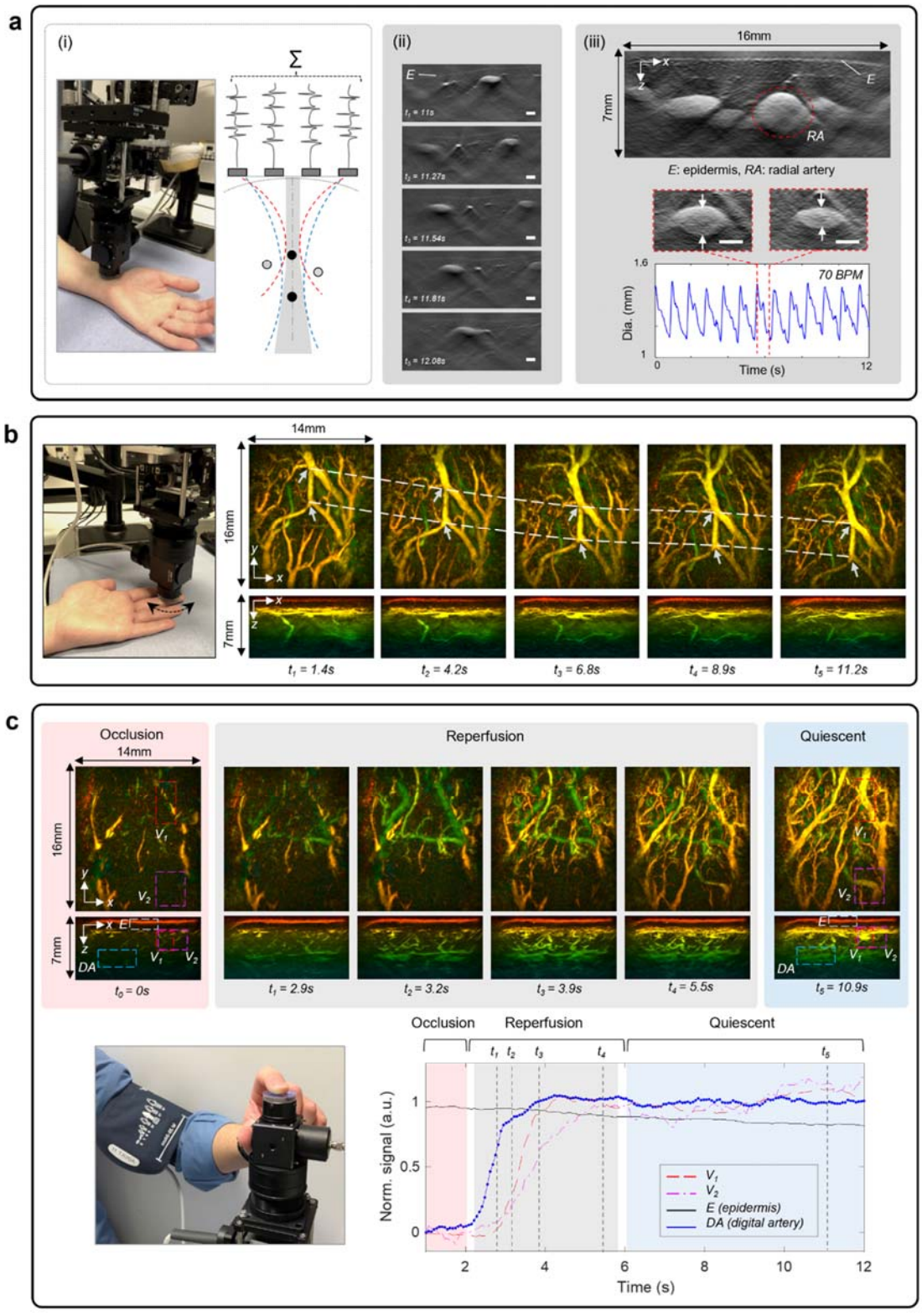

Figure 6: Dynamic PAT imaging: (a) Video rate 2D imaging, (i) *Left*; probe head positioned on wrist. *Right*; illustration of elevational receive beamforming, (ii) sequence of images of blood vessels in the wrist region acquired at different time points at a frame rate of 33 fps as probe head is moved across the skin surface from right to left; see Video 1 for complete image sequence. (iii) *Top;* image of radial artery (RA) and adjacent veins in the wrist. *Centre;* two images of compressed radial artery acquired 0.8s apart showing change in its dimensions due to pulsatile motion of blood flow; see Video 2 for complete image sequence. *Lower;* Oscillatory time-variation of radial artery size at 70 beats per minutes (BPM). Single frame scan-time T=30ms. (b) Real-time 3D imaging. Images acquired at 6 different time points as the finger-tip is translated across the probe

head. The pair of white dotted lines shows the translational trajectory of two vessel bifurcations identified by white arrows. See Video 4 for complete image sequence. (c) Haemodynamic response due to arterial cuff occlusion. *Top;* images of finger-tip vasculature acquired at 5 different time points showing occlusion, reperfusion and quiescent phases. See Video 5 for complete image sequence. *Lower;* time course of vascular signal in ROIs delineated by dotted rectangles corresponding to two vessel regions (V1 and V2), the epidermal region (E) and the digital artery (DA). Scale bars: 1mm. Imaging parameters: λ=850nm, PRF=200Hz, N=64, A-line rate 12,800 Lines/s, dx=dy=162μm, dt=16.67ns

In a second experiment, the radial artery (Figure 6a(iii)) was imaged at 33fps enabling the time-varying change in its dimensions due to the pulsatile motion of the blood flow to be visualised. This is illustrated in Video 2 with Figure 6a(iii) showing a plot of the oscillatory variation in the minor axis of the compressed artery at a frequency corresponding to the physiologically normal 70 beats per minute. In the examples shown in Figure 6a the photoacoustic time-series data were downloaded following the scan and the images reconstructed and visualised offline. Video 3 shows an example where images of the skin vasculature were reconstructed and visualised online in real time as the probe head is translated across the skin surface. This incurs a modest time-penalty compared to offline reconstruction due to the limited data transfer speed from the memory of the RF digitiser card resulting in a reduced frame rate of 25 fps.

3D dynamic imaging

To illustrate the dynamic 3D imaging capability of the system, two experiments were undertaken. In the first, a sequence of images was acquired as the probe head was translated over the surface of the finger-tip and are shown Video 4. Five representative frames reconstructed from the data used to produce this Video are shown in figure 5b. They correspond to different time points during the motion of the probe with the white dotted lines showing the translational trajectory of a pair of vessel bifurcations (white arrows). To acquire the data for these images, the scan area was continuously scanned over a period of 12s according to a pre-determined randomised spatial pattern acquiring a total of 153,600 A-lines. Each of the images in figure 5b was reconstructed from 7680 A-lines acquired in 0.6s. To provide a smooth dynamic visualisation in Video 4, a sliding window advanced in increments of 10% was applied to the entire measured photoacoustic data set. Thus, the first frame was reconstructed from the first 7680 A-lines. To reconstruct the second frame, the first 768 A-lines (the first 10%) were replaced by the A-lines numbered 7681 to 8449 (the next 10%) and so on with the window advancing incrementally by 10% until it reaches the end of the complete 153,600 A-line measured data set. Video 4 therefore comprises 200 frames acquired over 12s with a frame rate of 16.7 fps; the latter is termed the “refresh frame rate” since each frame is an update of the previous one with just 10% new A-line data rather than being formed from an entirely new set of A-lines. In this example, the reconstruction and visualisation of the images was performed offline following acquisition of the complete data set. However, real-time dynamic imaging can also be performed online in 3D to facilitate ROI localisation and probe positioning. This is shown in Video 5 which shows the probe head being translated across the palm but in this case the 3D images are reconstructed and displayed in real-time using a 50% sliding window with a refresh frame rate of 3fps.

In the second experiment, an invoked haemodynamic response was visualised. This was achieved by placing an inflatable cuff around the upper arm of a volunteer and inflating it to a pressure of 230mmHg for 5 seconds to produce an arterial occlusion thereby temporarily reducing perfusion in the downstream digital microvasculature. Following the release of the cuff, the vasculature is rapidly re-perfused achieving a steady-state thereafter. These changes were visualised by placing the forefinger tip on the sensor and continuously randomly scanning the sensor for a period of 12 seconds. Video 6 shows the complete image data set, reconstructed and visualised with a 16.7 fps refresh frame rate using the previously described 10% sliding window method. Figure 6c shows a sequence of six image frames corresponding to the occlusion, re-perfusion and quiescent periods. In addition, the temporal evolution of the mean image intensity within ROIs corresponding to the epidermis (E), two regions of the vasculature (V1 and V2) and the digital artery (DA) are plotted. These results show that during the occlusion period, the contrast exhibited by the vasculature is weak. When the cuff is released, rapid re-perfusion occurs and the contrast increases attaining its normal level within 2-3 seconds. The rate of increase is similar for all three vascular ROIs (V1, V2 and DA) although the onset

time for each is different; the signal corresponding to digital artery (DA) is the first to increase, as expected since it is the arterial flow that resumes first, followed by V1 and V2. Notably, the signal corresponding to the epidermis is relatively constant over time which is consistent with the assumption that the contrast in this region is predominantly non vascular, originating from dermal melanin rather than blood. The ability to visualise hemodynamic events in this way could enable the study of time-varying physiological responses such as post-occlusive reperfusion, pressure-induced vasodilation or thermal reflex events[54]. This could potentially be utilised for the clinical assessment of patients with diabetes and other diseases associated with impaired microvascular reactivity[55,56].

Exploratory clinical case studies

To illustrate how the scanner could be used clinically, exploratory case studies on patients with suspected vascular changes associated with peripheral vascular disease, skin inflammation and rheumatoid arthritis were undertaken (see Methods). These are preliminary studies not intended to provide a clinical validation of the technology but illustrate potential areas of application that warrant future more comprehensive clinical studies.

Peripheral vascular disease: Peripheral vascular disease (PVD) affects more than 25 million individuals across the USA and Europe[57] and is a complication of diseases such as diabetes that can lead to compromised perfusion resulting in pain, tissue damage and in severe cases necessitates limb amputation. While larger vessels can be visualised using conventional duplex ultrasound or MRI, the small vessel changes implicated in PVD that can contribute to adverse clinical consequences such as poor wound healing and amputation can not be visualised in sufficient detail. Hence there is a need for novel sensitive label-free imaging techniques that can be used to detect nascent microcirculatory changes and prompt the early intervention required to prevent the onset of tissue damage. It has been suggested that PAT could play a role in this context[17,18]. To illustrate the potential utility of the scanner in PVD, the feet of patients at risk of small vessel PVD were imaged in the vicinity of the Dorsalis Pedis Artery (DPA). Following clinical examination, the microcirculation in the right foot of a patient (denoted Patient 1) was assessed as normal whereas the left foot was symptomatic of impaired perfusion. The PAT image of the unaffected right foot of this patient (Figure 7a(i)) appears broadly consistent with the images acquired in disease-free volunteers. The affected left foot (Figure 7aii) however exhibits differences with evidence of vessel tortuosity which has been linked to microvasculopathy associated with PVD[58]. Figures 7b and 7c show PAT images of two patients with Type 2 diabetes which is commonly associated with PVD. Patient 2 was diagnosed with mild disease and exhibits an apparently normal vascular morphology. The PAT image of Patient 3, who was diagnosed with more severe disease, reveals a more disorganised, irregular microvascular architecture with several tortuous vessels, some exhibiting a corkscrew structure (Figure 7c) which in retinal vessels has been linked with diabetes[59,60]. The ability to visualise the lower limb microvasculature in detail in this way could be used to study small vessel-PVD linked to diseases such as diabetes with a view to identifying clinically-relevant structural microvascular biomarkers for informing diagnosis and treatment decision making.

Inflammation: Visualising angiogenesis induced by inflammation is relevant to the assessment of a variety of disease and injury processes, amongst them dermatological conditions, cancer and rheumatoid arthritis. To illustrate the potential application of the scanner in this context, it was used to image three examples of inflammation-driven neovascularisation. Figure 8a shows the first of these. Images were acquired longitudinally at 5 different time points of a region of superficial skin inflammation around a raised papule on the forearm following a suspected insect bite. Images were acquired at different times over a period of 7 days during which the papule was judged to be visible

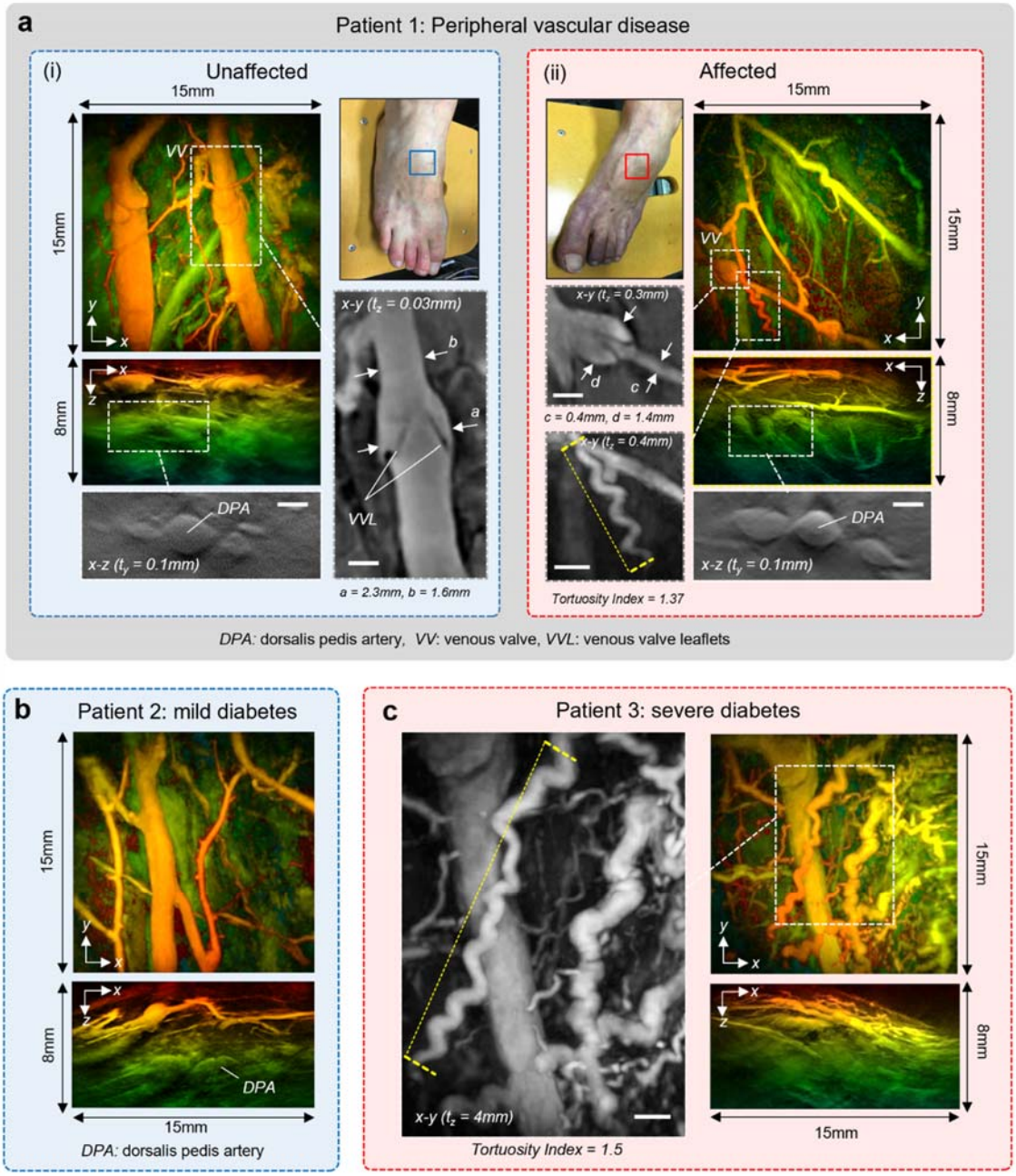

Figure 7: PAT images of feet of patients with suspected peripheral vascular disease (PVD). (a) Patient 1: (i) Unaffected right foot. *Left;* x-y and x-z depth-to-colour encoded MIPs. Expanded view greyscale MIPs: *Lower;* x-z MIP showing Dorsalis Pedis Artery (DPA). *Right;* x-y MIP showing venous valve. (ii) Affected left foot. *Right;* x-y and x-z depth-to-colour encoded MIPs. Expanded view grayscale MIPs showing *Left;* venous valve. *Lower;* corkscrew vessel, Tortuosity Index=1.37 (measured over length of vessel indicated by yellow dotted line), *Lower right:* greyscale x-z MIP showing DPA. (b) Patient 2: mild Type 2 Diabetes, x-y and x-z depth-to-colour encoded MIPs, (c) Patient 3: severe Type 2 Diabetes, *Right;* x-y and x-z depth-to-colour encoded MIPs, *Left; e*xpanded view grayscale MIP showing disorganised irregular vasculature and corkscrew vessel with Tortuosity Index=1.5 (measured over length of vessel indicated by yellow dotted line). Scale bars: 1mm. t_x and t_y: slice thicknesses of y-z and x-z greyscale MIPs respectively. Imaging parameters: λ=850, dx=dy=108μm, dt=16.67ns, PRF=100Hz, N=16, A-line rate: 1400 A lines/s, scan-time T=15s.

by eye. An additional image was acquired 38 days later when the inflammation had fully subsided. The image on day 1 was acquired when the inflammation was judged to be at its apogee. It reveals a dense, chaotic microvascular architecture in the region of the papule that extends from the epidermis to the hypodermis to a depth of approximately 4 mm. Visual inspection of the sequence of images in figure

8a shows the number of vessels in this region gradually diminishing to the presumed baseline over time. This is evidenced quantitatively by the reduction in the vascular density V_s of the inflamed region from 28% to 8%, where V_s is the percentage of the image volume occupied by vessels (see Methods). These results illustrate how the scanner can visualise and quantify changes in the microvascular architecture of the skin over time, attributes that are relevant to the clinical assessment of inflammatory skin disorders such as eczema or dermatitis[19].

In the second example, the scanner was used to visualise the skin inflammation linked to breast cancer. This can arise when a tumour provokes an inflammatory response that produces skin neovascularisation in, for example, the nipple areolar complex (NAC) region. In patients with locally advanced disease of this nature, even if the tumour is beyond the penetration depth range of the scanner, the neovascularisation can be relatively superficial (<5mm). This is illustrated in figure 8b. Figure 8b(ii) shows PAT images acquired in different areas (B2, B3, B4) of the NAC region in a patient with a tumour in the right breast, identified via diagnostic ultrasound and MRI. Compared to the PAT image of the unaffected left breast (Figure 8b(i)), the images of the right breast reveal an increase in contrast due to skin neovascularisation, also evident in the MR images but not via ultrasound examination or visual inspection. Image contrast in the inflamed region was quantified by calculating V_s as described above with the ROI selected to exclude the skin and nipple. For the unaffected left breast, V_s=6% whereas the mean V_s of the three images of the inflamed region in the right breast was 26%. Although the objective was not to visualise the tumour, its boundary is discernible in the x-z MIP for position B4; Suppl. Fig 3 provides additional visualisations of this region showing the tumour and its supplying vasculature. The ability to visualise inflammatory responses in this way could find application, for example in the study of the aetiology of tumour driven inflammation in cancer.

In the third example, the scanner was used to image the joints of patients with rheumatoid arthritis. This is a disease of the joints characterised by inflammation of the synovial membrane which affects >20 million people worldwide[61], causing discomfort, immobility and, if left untreated, loss of joint use. The inflammation produces neovascularisation that could potentially serve as a marker of disease severity but is inadequately visualised by existing modalities such as conventional B-mode and Doppler ultrasound. This has led to suggestions that PAT could play a role in the clinical assessment of rheumatoid arthritis[20,21,22.]. To illustrate the potential application of the scanner in this context, images of suspected inflamed hand joints were acquired.

Figure 8c shows examples of PAT images of the interphalangeal joints in a patient with a diagnosis of rheumatoid arthritis in the right hand; the diagnosis was based on the observation of synovial thickening and blood flow observed under clinical Duplex ultrasound examination, a biochemical inflammatory marker and patient-reported symptoms. Consider the vertical x-z and y-z MIPs in figure 8c. Compared to the image of the unaffected joint in the left hand of the same patient (figure 8c(i)), the affected joint in the tendon region (indicated by the white dotted ellipse in figure 8c(ii)) exhibits increased contrast. Given the more subtle nature of the contrast compared to that evident in figures 8a and 8b, this preliminary observation was consolidated by undertaking a more extensive study. This involved scanning 17 joints of a further 7 patients with high disease activity (>5.1 DAS28 score)) and 44 joints of a control group of 5 healthy volunteers below the age of 30 yrs. The vascular contrast in the synovial region was then quantified by calculating the mean intensity V_I of the pixels above the noise floor (see Methods). This approach was used instead of the vessel-by-vessel based analysis used in the examples shown Figures 8a and 8b to estimate V_s. This is because joint inflammation was observed to manifest itself over time as an increase in sub-resolution spatially averaged vascular contrast, rather than a proliferation of clearly resolved individual vessels. The results are summarised in the box-whisker plot in figure 8, which show a significant difference ($p<0.01$) between the patient group with active disease (median V_i =141314) and the volunteer control group (mean V_I=39,511). This suggests that even subtle sub-resolution inflammation-driven neoangiogenesis can be detected, as well as that associated with the clearly resolvable changes in microvascular morphology observed in figures 8a and 8b.

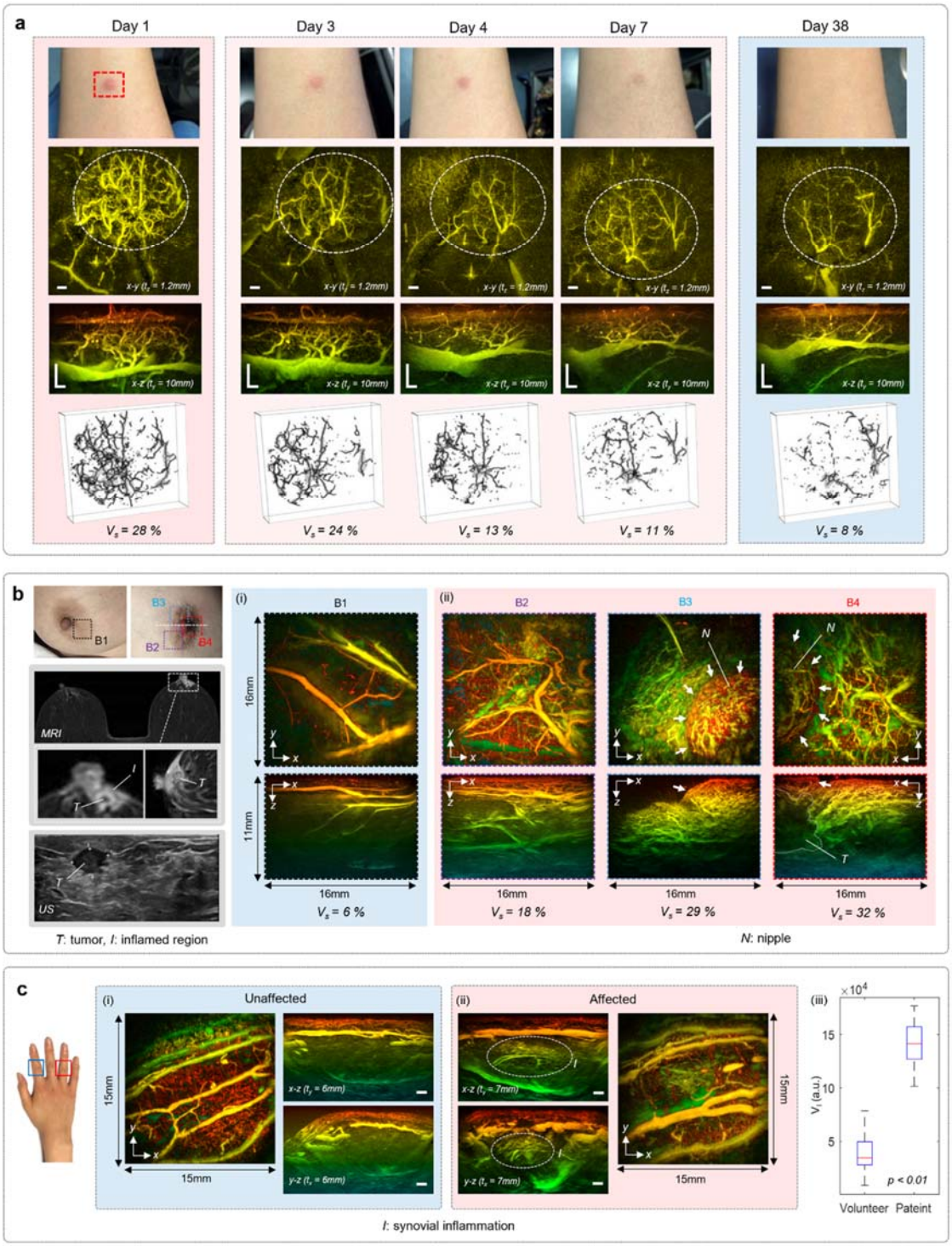

Figure 8: PAT images of inflammatory responses. (a) Inflammation around raised skin papule over 38 days. x-y depth-to-colour encoded MIPs (1.2 mm slice thickness; z=0.5mm – 1.7mm) and x-z MIPs. The inflamed regions are indicated by the dotted white ellipses. Photograph in blue panel is representative of imaged region at day 38 but was taken non-contemporaneously at a later date. Lower row of images show 3D skeleton representations of vascular architecture used to estimate vascular density, V_s. Scale bars: 1mm. t_z and t_y: slice thickness of x-y and x-z greyscale MIPs. Imaging parameters: λ=850, dx=dy=108µm, dt=16.67ns, PRF=100Hz, N=64, A-line rate: 3723 A lines/s, scan-time T=5.5s. **(**b) Inflammation in nipple areolar complex (NAC) region of patient with tumour in right breast. *Left panel:* Photographs, MRI and ultrasound images. MRI images; *top;* full view, *bottom;* expanded view around NAC region of affected right breast showing inflamed region (I) and tumour (T). Ultrasound image showing tumour. (i) PAT image (x-y and x-z depth-to-colour encoded MIPs) of region B1 on unaffected breast showing low microvascular density, V_s=6%. (ii) B2, B3 and B4 are locations on the affected breast showing increased vascular densities, V_s= 18%, 29%, 32% respectively. White arrows delineate nipple (N). White dotted line

on B4 x-z MIP image represents presumed tumour boundary; see Suppl Inf. Fig 3 for additional tumour visualisation. Imaging parameters: λ=850, dx=dy=108µm, dt=16.67ns, PRF=100Hz, N=16, A-line rate: 1400 A lines/s, scan-time T=15s. (c) Inflammation in synovial region of finger joints in patient with rheumatoid arthritis. (i) Unaffected proximal interphalangeal joint on index finger. x-y, x-z and y-z depth-to-colour encoded MIPs. (ii) Affected proximal interphalangeal joint on ring finger. x-y, x-z and y-z depth-to-colour encoded MIPs. x-z and and y-z MIPs show increased vascular contrast in inflamed synovial region (indicated by white dotted ellipses). *Right:* Box and whisker plot showing differences in mean vascular signal V_I for unaffected (44 joints from 5 healthy volunteers) and affected (17 disease active joints from 7 patients) joints. t_x and t_y: slice thicknesses of y-z and x-z greyscale MIPs respectively. Imaging parameters: λ=850, dx=dy=108µm, dt=16.67ns, PRF=100Hz, N=16, A-line rate: 1400 A lines/s, scan-time T=15s. All scale bars: 1mm.

DISCUSSION

A high resolution 3D photoacoustic scanner based on the FP ultrasound sensor concept has been developed and evaluated to assess its potential as a tool for clinical vascular imaging. The key engineering advance that has been made relates to acquisition speed. Early generation FP scanners provided high 3D image quality but at the cost of long scan-times, thus precluding practical clinical use. This limitation has been overcome by variously parallelising the FP sensor read-out, operating at high PRFs and employing compressed sensing. High quality 3D images can now be acquired without compromising image quality in a few seconds rather than the several minutes of early scanners with even shorter scan-times of a few hundred ms achievable with modest reductions in image fidelity or lateral FOV. The significant acceleration in acquisition speed achieved has transformed the clinical applicability of the technology. It now enables high quality in vivo images to be repeatably acquired without appreciable motion-related artefacts, permits real-time image display during probe positioning and allows the visualisation of time-varying perfusion and other haemodynamic events. Moreover, the scanner has been shown to be a reliable and versatile instrument that can provide high fidelity in vivo images at a diversity of anatomical sites with comparable patient acceptability and convenience to a conventional clinical ultrasound scanner. All of this sets the scene for the clinical translation of the technology as a tool for the assessment of diseases characterised by microvascular changes.

Clinical applications

This study has shown that the scanner can provide rapid, highly detailed volumetric images of vascular anatomy and function. This is evidenced by the imaging studies on healthy volunteers which demonstrated that high resolution 3D images to depths approaching 15 mm can be acquired revealing capillaries, venules, arterioles and large mm-scale arteries and veins as well as other structures such as venous valves, skin sulci and hair follicles. In addition, the clinical case studies showed that the geometrical parameters of the superficial vasculature could be quantified and followed longitudinally over time. Moreover, these studies illustrated how disease-specific changes can be visualised; increased vessel tortuosity which is associated with PVD and the neovascularisation associated with inflammation in the skin and hand joints were visualised and quantified. All of this suggests there is a potentially rich source of structural vascular biomarkers available that could inform the detection, diagnosis and treatment monitoring of a wide range of disease and injury processes characterised by microcirculatory abnormalities.

In cardiovascular medicine, the scanner could be used to provide early detection of the skin microvascular changes associated with PVD that precede tissue damage in the lower limb in patients with diabetes. This could provide more effective monitoring for planning therapeutic interventions such as angioplasty before tissue death and ulceration occurs. As shown in the current study, the technology also lends itself to the assessment of inflammatory conditions. In patients with rheumatoid arthritis it could be used to assess synovial inflammation to identify which patients require treatment and monitor them over time to ensure optimal dosing in order to minimise damage and loss of joint mobility. In a similar fashion, it could be used for the assessment of inflammatory skin conditions such as eczema or dermatitis and inflammation associated with cancer, infection and superficial soft-tissue injury due to burns or wounds. A further promising area is surgical guidance[62]. Reconstructive procedures such as flap surgery require detailed knowledge of the vasculature in and around the transplanted tissue. The scanner could therefore be used preoperatively to identify perforators to aid

selection of the optimum donor tissue site, intraoperatively to guide flap positioning to ensure adequate connection between the donor and acceptor vascular networks and post-operatively to monitor perfusion and guide recovery. Similarly, it could be used in cancer surgery to delineate the margins of superficial vascularised tumours in the skin or oral cavity and help plan their surgical excision. In open or laparoscopic surgery, the latter enabled by endoscopic implementations[63,64], it could be used intraoperatively to guide the treatment of tumours in the liver and other abdominal organs or surgical procedures in the GI tract.

Future technical developments

The FP sensor technology is versatile and flexible with considerable scope to adjust acquisition speed, resolution, penetration depth, functionality and form factor. In this sense, it can be regarded as a generic platform technology around which a range of imaging instruments, each tailored to meet the requirements of specific applications could be developed.

For example, scanners operating at higher frame rates than demonstrated in the current study could be realised in several ways for applications that require visualising dynamic vascular biomarkers. Increasing the sensor read-out parallelisation by a factor or 2-3 would provide a commensurate increase in frame rate to ~5fps without compromising image quality. Although higher levels of parallelisation with the current multibeam read-out architecture are likely to be prohibitive in terms of technical complexity and cost, alternative full-field massively parallelised camera read-out schemes could mitigate this[65]. Accelerating scan-speed by operating at high (kHz) PRFs is also possible; laser diode arrays providing kHz PRFs with mJ scale pulse energies at more deeply penetrating wavelengths such as 800nm than the 1064nm wavelength of the 1kHz PRF fibre laser used in the current study are available commercially. Inevitably however, increasing PRF incurs an SNR cost due to the need to limit the pulse energy to comply with safe laser exposure limits. Sub-sampled acquisition provides an opportunity to address this. As shown in figure 5, surprisingly high quality images can be reconstructed with even highly sub-sampled data, albeit at the cost of long image reconstruction computation times although there is scope to reduce this using learned reconstruction methods[52]. Taking all of the above into account, a 3D frame rate of 10fps can reasonably be expected without significantly compromising image quality via a combination of a factor of 2 increase in parallelisation and a modest sub-sampling of a factor of 2 or 3. For applications that can tolerate a reduction in image SNR, a combination of x10 sub-sampling and a 1kHz PRF could enable 3D frame rates in excess of 100 fps.

Penetration depth and spatial resolution can be adjusted by modifying the FP sensor design. It has been shown that, by increasing the sensor finesse though the use a plano-concave cavity geometry[66,31] , detection sensitivity can be increased by at least an order of magnitude offering the prospect of increasing imaging depth to 2-3 cm. The acoustic bandwidth can readily be increased to 100MHz by reducing the FP polymer film thickness to achieve higher spatial resolution for ultra-high resolution vascular imaging applications, for example, visualising the highly superficial dermal vasculature at capillary level.

Other imaging modalities can readily be incorporated to provide complementary anatomical or physiological information. The transparent nature of the sensor allows straightforward integration of pure optical imaging techniques such as OCT[67] or fluorescent imaging. A 3D ultrasound imaging capability[68] could be implemented by using dichroic absorptive coating deposited on the sensor. This would enable a dual-mode imaging modality in which the ultrasound image provides morphological mechanical contrast complementary to the PAT vascular contrast. As well as visualising anatomical features indistinguishable with PAT, it would aid clinical translation by providing an anatomical imaging landscape recognisable to clinicians familiar with ultrasound that aids orientating and interpreting the PAT image.

Finally, the concept lends itself to a multitude of form factors. The large size and weight of the current galvanometer based probe-head makes it somewhat cumbersome for routine clinical use. By replacing the galvanometer scanners with a compact MEMs based scanner, a hand-held probe head of similar dimensions, ergonomic shape and weight to a conventional clinical ultrasound probe could be realised. Moreover, there is scope to develop miniature endoscopic or intracavitary probes by interrogating the FP sensor via an optical fibre bundle[63,64]. Not least, by virtue of the all-vacuum deposition fabrication techniques used to manufacture the sensor which enables batch fabrication at

low unit cost, the technology lends itself to minimally invasive applications where single-use disposable sensors are required.

CONCLUSION

A high fidelity 3D PAT scanner has been demonstrated that can provide rapid, detailed *in vivo* 3D images of superficial vascular anatomy with clinically relevant acquisition times. The level of image detail it provides suggests it could find application as a tool for the clinical detection, diagnosis and treatment monitoring of diseases such as diabetes or cancer that are characterised by microcirculatory abnormalities. The demonstrated high image fidelity, fast acquisition, design versatility and practical nature of the technology sets the scene for its clinical translation in oncology, cardiovascular medicine, dermatology, image guided surgery and other medical specialities.

METHODS

Fabry Perot ultrasound sensors: The FPI spacer was formed by the vacuum deposition of Parylene C[69]. The mirrors of the FPI comprised a dichroic dielectric stack transparent between 560nm and 1300nm and highly reflective between 1460 nm and 1630 nm (see Suppl Figure 1). A Parylene C layer a few microns thick was deposited over the FPI to protect it from water ingress and mechanical damage. Two different sensors of similar design were used: for the volunteer studies, the sensor spacer thickness was 26.6 µm providing an estimated -3dB bandwidth of 31.5 MHz. For the clinical case studies, the sensor spacer thickness was 29.6 µm providing an estimated -3dB acoustic bandwidth of 27.6 MHz. The effective signal bandwidth was the same irrespective of the sensor used since a digital 50kHz-20MHz bandpass filter was applied to the detected photoacoustic waveforms in all cases, except for the high resolution scan-mode images (Fig 4) for which the filter bandwidth was 50kHz-60MHz. For the 26.6 µm sensor the reflectivity finesse was F=76.6, the fringe visibility V = 0.78 and the free-spectral-range FSR= 26.6nm. For the 29.6µm sensor, F = 33.8, V =1.00 and FSR=23.6nm

Scanner hardware: The interrogation laser system comprised a Santec external cavity laser, tunable between 1500nm and 1630nm amplified by a pair of C-band EDFAs. To record the output of the FP sensor, custom-designed InGAs photodiode-transimpedance units with ac and dc-coupled outputs were used; the bandwidth of the ac-coupled output was 50kHz - 75MHz. Each photodiode unit was connected to an input of a multichannel RF acquisition system of up to 64 channels with 60Ms/s sampling rate. Three excitation laser systems were variously used depending on the PRF requirements. Two were Type II 532nm pumped optical parametric oscillator (OPO) based laser systems. One was an Ekspla Photosonus-X operating at 100Hz (depicted in figure 1b) and the other was an Innolas EVO 200 that could operate at either 100Hz or 200Hz. Both provided pulse energies in excess of 10 mJ, pulse durations of 5ns and a signal wavelength range between 660nm and 1300nm. The outputs of both systems were coupled into 1.5mm diameter optical fibres. The third excitation laser was a large core Yb pulsed fibre laser based on a MOPA architecture[51] custom designed and built by the Optoelectronics Research Centre, Southampton University. It provided a 1064nm output, a pulse energy of 10mJ, adjustable pulse duration (10ns-500ns) and PRFs (100Hz-1kHz).

System characterisation. The system was characterised using similar methods to those described in reference 36. The NEP distribution shown in figure 1c was obtained by measuring the FP sensor signal at multiple scan points on the sensor in response to a plane wave of known peak pressure emitted by a calibrated planar 3.5MHz piezoelectric transducer. At each of the scan points (35,512 points for single beam read-out and 34,560 points for 64 beams read-out) the signal amplitude and rms noise (over a 20 MHz measurement bandwidth) were measured to estimate the NEP. The sensor frequency response (Figure 1c) was obtained using a substitution method based on a broadband laser generated ultrasound source and a calibrated reference detector of known frequency response. The *in vivo* acoustic frequency tissue spectrum shown in figure 1c was obtained by averaging the frequency spectra of 34,560 A-lines acquired in a scan of the human palm. The spatial resolution as function of position was estimated by scanning over 21 x 19.5 mm^2 a grid of plastic line absorbers immersed in

Intralipid using a scan step size dx=dy=108 µm. To estimate the lateral and vertical resolution, the edge spread and line spread functions respectively were measured[36].

Signal processing, image reconstruction and visualisation. Prior to image reconstruction, the raw photoacoustic waveforms were pre-processed by applying a 50kHz-20MHz bandpass filtering and spatially interpolating on to a x2 finer grid except for the dynamic imaging examples (Figure 5) for which a factor of x3 interpolation was used[70]. The tissue sound speed was then estimated using an autofocus method[71] and input to the reconstruction algorithm. All images except the sub-sampled images in figure 5b were reconstructed using a k-space backprojection algorithm[72]. The reconstructed image was then interpolated on to x2 finer grid. The image reconstruction was implemented using k-Wave, an open-source toolbox developed at UCL for the time-domain simulation and reconstruction of PA and ultrasound wave fields (www.k-wave.org[73]).

By employing a fast C++ CPU optimised computational implementation, image reconstruction time has been reduced by a factor of 5 over a previous Matlab implementation[73]. Reconstruction time depends on scan area, spatial sampling interval and the number of points in the time-record. For example, for a scan area of 21 x 19.5 mm^2, dx=dy=108µm and a record length of 600 time points, reconstruction time was 0.8s, decreasing to 0.48s for a 15 x 15 mm^2 scan for the same spatial-temporal sampling intervals using a desktop PC. The sub-sampled images in figure 5b were reconstructed using an iterative model based reconstruction algorithm based on least squares minimisation with a total variation regularisation term and a non-negativity constraint as described in[45]. Regularisation parameters were chosen to 1) suppress the most visible reconstruction artefacts 2) retain most visible small vessels and 3) correct the most obvious geometrical distortion of clearly visualised vessels. The regularisation parameters used were 10^{-3}, 1.2 x 10^{-3}, 3 x 10^{-4} and 1.5 x 10^{-4} for the sub-sampling factors 100%, 50%, 25% and 12.5% respectively. A maximum of 50 iterations were computed for each example. Computing the reconstruction of the palm images in Fig 5(b) (192x180x396 voxels) took 1h24m, 1h21m, 1h21m and 2h9m for the sub-sampling factors 100%, 50%, 25% and 12.5% respectively by using optimized CUDA code on a NVIDIA GTX Titan X Maxwell GPU.

Since the excitation beam diameter was larger than the scan area, in some cases, images were reconstructed slightly outside the scan-footprint to increase the lateral FOV - eg the images in figure 2c and 2d were reconstructed over a 22 x 22mm area although the physical scan-area was 21 x 19.5 mm^2. To aid the visualisation of deeper-lying features, the image intensity was normalized with respect to depth using an exponential function as a first-order correction for optical and acoustic attenuation. MIPs are displayed using a logarithmic image intensity scale. Unless otherwise indicated, all colour-to-depth encoded MIPs are full thickness projections whereas greyscale MIP are reduced thickness projections; t_x and t_y denote the x and y slice thicknesses respectively in these.

Image quantitation: The SNR of the images in figure 5 was estimated as follows. For the images in figure 5a, the signal was determined by estimating the mean image intensity above the noise floor within the volume demarcated by the white dotted rectangles. For the sub-sampled images in figure 5b the entire image volume was used to estimate the signal. In both cases, the noise was determined by selecting a volume devoid of image features and calculating the rms value of the pixel intensities within it. To quantify vascular contrast, two metrics were used. When individual vessels could be resolved (as in Figures 8a and 8b), the vascular density V_s which represents the percentage of the image volume occupied by resolvable vessels was used. V_s was estimated by segmenting the vasculature, forming a 3D skeleton visualisation and counting the number of non-zero pixels as a percentage of the total number of pixels. To quantify sub-resolution vascular contrast (as in Figure 8c), the mean intensity of the pixels above the noise floor within the volume of interest was estimated and denoted V_I. The tortuosity index (Figure 7) is given by the ratio of the vessel length to the straight line distance between two points along the vessel[60].

Volunteer and patient studies: Volunteers were recruited from the Department of Medical Physics and Biomedical Engineering at UCL with ethical permission granted by University College London

Research Ethics Committee (Project ID: 1133/001). Patients were recruited from relevant clinics at UCL Hospitals NHS Trust under NHS Research Ethics Committee approval (IRAS Project ID number: 206196). Written informed consents was obtained from all participants. All *in vivo* images were acquired using an incident laser fluence less than 4mJ/cm^2 in accordance with the maximum permissible exposure for skin defined by BS EN 60825-1[74] for the PRFs and exposure durations used.

Data availability

The raw image data sets and reconstructed image data are available from the authors for research purposes upon reasonable request.

Code availability

All custom Matlab scripts used to process and analyse the data are available from the authors for research purposes upon reasonable request.

Disclosures

PB, EZ and AP are shareholders in DeepColor Imaging SAS to whom the intellectual property associated with the FP sensor technology has been licensed. Deepcolor SAS were not involved in any aspect of the work reported in this publication.

Acknowledgements

The authors acknowledge funding from the following sources. H2020 ERC Advanced Grant (Ref 741149), CRUK-EPSRC (Ref C53954/A25285 and C53954/A26617), EPSRC (Ref EP/K009745/1, EP/J022144/1 and EP/T014369/1), Wellcome Trust/EPSRC (Ref NS/A000050/1 and 204841/Z/16/Z), the National Institute for Health Research University College London Hospitals Biomedical Research Centre (Ref: BRC/191/CN/AP/101330 and BRC658/HEI/PB/110410). The authors gratefully acknowledge the support of the following individuals: Katerina Soteriou and Teresita Beeston (UCL Hospitals NHS Foundation Trust) for managing the patient studies, Madhura Castelino and Conrad von Stempel (UCL Hospitals NHS Foundation Trust) for helpful discussions on inflammatory arthritis and peripheral vascular disease respectively, Bolin Pan for assistance with the iterative image reconstruction scripts and David Richardson, Shaiful Alam, Martin Berendt and Di Lin at the Optoelectronics Research Centre, Southampton University for developing the fibre laser system. The authors also acknowledge Jamie Guggenheim and Olumide Ogunlade for reviewing the manuscript.

Author Contributions

NTH designed, constructed and characterised the multibeam scanner, developed the image analyses methods and performed the volunteer and patient imaging studies. EZ designed and fabricated the FP sensors and was responsible for the original FP scanner concept. OF, OA and AP designed and performed the patient imaging studies and provided the clinical interpretation of the images. FK and JJ were responsible for the C++ implementation of the k-space image reconstruction algorithm. JZ reconstructed the sub-sampled images and contributed to the image analysis methods. TA operated the fibre laser and contributed to the imaging experiments. FL, SA and MB developed the sub-sampled image reconstruction mathematics and their computational implementation. BC contributed to the image reconstruction methods and aspects of the scanner implementation. PB contributed to the scanner and sensor development, the overall study design and co-wrote the manuscript. All authors contributed to the preparation and review of the manuscript.

REFERENCES

[1] William D. James, Dirk Elston, James R. Treat, Misha A. Rosenbach, Andrews' Diseases of the Skin, Clinical Dermatology, 13th Edition - January 18, 2019

[2] Chao, C. Y. L., & Cheing, G. L. Y. (2009). Microvascular dysfunction in diabetic foot disease and ulceration. Diabetes/Metabolism Research and Reviews, 25(7), 604–614.
[3] Paul, D. W., Ghassemi, P., Ramella-Roman, J. C., Prindeze, N. J., Moffatt, L. T., Alkhalil, A., & Shupp, J. W. (2015). Noninvasive imaging technologies for cutaneous wound assessment: A review. Wound Repair and Regeneration, 23(2), 149–162.
[4] Allen, J., & Howell, K. (2014). Microvascular imaging: techniques and opportunities for clinical physiological measurements. Physiological Measurement, 35(7), R91–R141.
[5] Deegan, A. J., & Wang, R. K. (2019). Microvascular imaging of the skin. Physics in Medicine & Biology, 64(7), 07TR01.
[6] Tanter, M., & Fink, M. (2014). Ultrafast Imaging in Biomedical Ultrasound. IEEE Trans. Ultrason. Ferroelectr. Freq. Control, 61(1), 102–119.
[7] Soloukey, S., Vincent, A. J. P. E., Satoer, D. D., Mastik, F., Smits, M., Dirven, C. M. F., … Kruizinga, P. (2020). Functional Ultrasound (fUS) During Awake Brain Surgery: The Clinical Potential of Intra-Operative Functional and Vascular Brain Mapping. Frontiers in Neuroscience, 13(January), 1–14.
[8] Beard, P. (2011). Biomedical Photoacoustic Imaging. Interface Focus, 1(4), 602–631.
[9] Su, R., Ermilov, S., Liopo, A., & Oraevsky, A. (2013). Laser optoacoustic tomography: Towards new technology for biomedical diagnostics. Nuclear Instruments and Methods in Physics Research, Section A: Accelerators, Spectrometers, Detectors and Associated Equipment, 720, 58–61.
[10] Wang, L. V, & Yao, J. (2016). A practical guide to photoacoustic tomography in the life sciences. Nature Methods, 13(8), 627–638.
[11] Taruttis, A., van Dam, G. M., & Ntziachristos, V. (2015). Mesoscopic and Macroscopic Optoacoustic Imaging of Cancer. Cancer Research, 75(8), 1548–1559. https://doi.org/10.1158/0008-5472.CAN-14-2522
[12] Li, D., Humayun, L., Vienneau, E., Vu, T., & Yao, J. (2021). Seeing through the Skin: Photoacoustic Tomography of Skin Vasculature and Beyond. JID Innovations, 1(3), 100039.
[13] Li, M., Tang, Y., & Yao, J. (2018). Photoacoustic tomography of blood oxygenation: A mini review. Photoacoustics, 10(May), 65–73.
[14] Lin, L., & Wang, L. V. (2022). The emerging role of photoacoustic imaging in clinical oncology. Nature Reviews Clinical Oncology, 19(6), 365–384. https://doi.org/10.1038/s41571-022-00615-3
[15] Valluru, K.S., Wilson, K.E. and Willmann, J.K. 2016. "Photoacoustic Imaging in Oncology: Translational Preclinical and Early Clinical Experience", *Radiology*, **280(2)**, 332-349
[16] Karlas, A., Fasoula, N. A., Paul-Yuan, K., Reber, J., Kallmayer, M., Bozhko, D., … Ntziachristos, V. (2019). Cardiovascular optoacoustics: From mice to men – A review. Photoacoustics, 14(March), 19–30.
[17]Karlas, A., Masthoff, M., Kallmayer, M., Helfen, A., Bariotakis, M., Fasoula, N. A., … Wildgruber, M. (2021). Multispectral optoacoustic tomography of peripheral arterial disease based on muscle hemoglobin gradients—a pilot clinical study. Annals of Translational Medicine, 9(1), 36–36. https://doi.org/10.21037/atm-20-3321
[18] Yang, J., Zhang, G., Shang, Q., Wu, M., Huang, L., & Jiang, H. (2020). Detecting hemodynamic changes in the foot vessels of diabetic patients by photoacoustic tomography. Journal of Biophotonics, 13(8), 1–11.
[19] Zabihian, B., Weingast, J., Liu, M., Zhang, E., Beard, P., Pehamberger, H., … Hermann, B. (2015). In vivo dual-modality photoacoustic and optical coherence tomography imaging of human dermatological pathologies. Biomedical Optics Express, 6(9), 3163.
[20] van den Berg, P. J., Daoudi, K., Bernelot Moens, H. J., & Steenbergen, W. (2017). Feasibility of photoacoustic/ultrasound imaging of synovitis in finger joints using a point-of-care system. Photoacoustics, 8, 8–14.
[21] Jo, J., Tian, C., Xu, G., Sarazin, J., Schiopu, E., Gandikota, G., & Wang, X. (2018). Photoacoustic tomography for human musculoskeletal imaging and inflammatory arthritis detection. Photoacoustics, 12(June), 82–89.
[22] Rajian, J. R., Shao, X., Chamberland, D. L., & Wang, X. (2013). Characterization and treatment monitoring of inflammatory arthritis by photoacoustic imaging: a study on adjuvant-induced arthritis rat model. *Biomedical Optics Express*, *4*(6), 900–908.
[23] Nam, S. Y., Chung, E., Suggs, L. J., & Emelianov, S. Y. (2015). Combined Ultrasound and Photoacoustic Imaging to Noninvasively Assess Burn Injury and Selectively Monitor a Regenerative Tissue-Engineered Construct. Tissue Engineering. Part C, Methods, 21(6), 557–566.
[24] Mantri, Y., Mishra, A., Anderson, C. A., & Jokerst, J. V. (2022). Photoacoustic imaging to monitor outcomes during hyperbaric oxygen therapy: validation in a small cohort and case study in a bilateral chronic ischemic wound. Biomedical Optics Express, 13(11), 5683.
[25] Zhang, H. F., Maslov, K., Stoica, G. & Wang, L. V. 2006 Functional photoacoustic microscopy for high-resolution and noninvasive in vivo imaging. Nat. Biotechnol. 24, 848–851
[26] Aguirre, J., Schwarz, M., Garzorz, N., Omar, M., Buehler, A., Eyerich, K., & Ntziachristos, V. (2017). Precision assessment of label-free psoriasis biomarkers with ultra-broadband optoacoustic mesoscopy. Nature Biomedical Engineering, 1(May), 0068.

[27] Tadayon, M. A., Baylor, M. & Ashkenazi, S. Polymer waveguide Fabry-Perot resonator for high-frequency ultrasound detection. IEEE Trans. Ultrason. Ferroelectr. Freq. Control 61, 2132–2138 (2014)

[28] Preisser, S. et al. All-optical highly sensitive akinetic sensor for ultrasound detection and photoacoustic imaging. Biomed. Opt. Express 7, 4171 (2016).

[29] Hajireza, P., Krause, K., Brett, M. & Zemp, R. Glancing angle deposited nanostructured film Fabry-Perot etalons for optical detection of ultrasound. Opt. Express 21, 6391–400 (2013).

[30] Yakovlev, V. V. et al. Ultrasensitive non-resonant detection of ultrasound with plasmonic metamaterials. Adv. Mater. 25, 2351–2356 (2013)

[31] Guggenheim, J. A., Li, J., Allen, T. J., Colchester, R. J., Noimark, S., Ogunlade, O., … Beard, P. C. (2017). Ultrasensitive plano-concave optical microresonators for ultrasound sensing. Nature Photonics, 11(11), 714–719

[32] Li, H., Dong, B., Zhang, Z., Zhang, H. F. & Sun, C. A transparent broadband ultrasonic detector based on an optical micro-ring resonator for photoacoustic microscopy. Sci. Rep. 4, 4496 (2014).

[33] Shnaiderman, R., Wissmeyer, G., Ülgen, O., Mustafa, Q., Chmyrov, A., & Ntziachristos, V. (2020). A submicrometre silicon-on-insulator resonator for ultrasound detection. Nature, 585(7825), 372–378

[34] Westerveld, W. J., Mahmud-Ul-Hasan, M., Shnaiderman, R., Ntziachristos, V., Rottenberg, X., Severi, S., & Rochus, V. (2021). Sensitive, small, broadband and scalable optomechanical ultrasound sensor in silicon photonics. Nature Photonics, 15(5), 341–345.

[35] Harary, T., Hazan, Y., & Rosenthal, A. (2023). All-optical optoacoustic micro-tomography in reflection mode. Biomedical Engineering Letters.

[36] Zhang, E., Laufer, J. & Beard, P. Backward-mode multiwavelength photoacoustic scanner using a planar Fabry-Perot polymer film ultrasound sensor for high-resolution three-dimensional imaging of biological tissues. Appl. Opt. 47, 561–577 (2008).

[37] Laufer, J., Johnson, P., Zhang, E., Treeby, B., Cox, B., Pedley, B., & Beard, P. (2012). In vivo preclinical photoacoustic imaging of tumor vasculature development and therapy. Journal of Biomedical Optics, 17(5), 056016-1-056016–056018.

[38] Ogunlade, O., Johnson, S. P., Lythgoe, M. F., Beard, P., & Pedley, R. B. (2019). Longitudinal Photoacoustic Imaging of the Pharmacodynamic Effect of Vascular Targeted Therapy on Tumors. *Clinical Cancer Research*, *25*(10), 7436–7448.

[39] Ogunlade, O., Connell, J. J., Huang, J. L., Zhang, E., Lythgoe, M. F., Long, D. A., & Beard, P. (2018). In vivo three-dimensional photoacoustic imaging of the renal vasculature in preclinical rodent models. *American Journal of Physiology-Renal Physiology*, *314*(6), F1145–F1153.

[40] Huynh, N., Ogunlade, O., Zhang, E., Cox, B., & Beard, P. (2016). Photoacoustic imaging using an 8-beam Fabry-Perot scanner. In Proceedings of SPIE (Vol. 9708, p. 97082L). https://doi.org/10.1117/12.2214334

[41] Plumb, A. A., Huynh, N. T., Guggenheim, J., Zhang, E., & Beard, P. (2018). Rapid volumetric photoacoustic tomographic imaging with a Fabry-Perot ultrasound sensor depicts peripheral arteries and microvascular vasomotor responses to thermal stimuli. European Radiology, 28(3), 1037–1045.

[42] Jathoul, A. P., Laufer, J., Ogunlade, O., Treeby, B., Cox, B., Zhang, E., … Beard, P. (2015). Deep in vivo photoacoustic imaging of mammalian tissues using a tyrosinase-based genetic reporter. Nature Photonics, 9(April), 239–246.

[43] Märk, J., Dortay, H., Wagener, A., Zhang, E., Buchmann, J., Grötzinger, C., … Laufer, J. (2018). Dual-wavelength 3D photoacoustic imaging of mammalian cells using a photoswitchable phytochrome reporter protein. Communications Physics, 1(1), 3.

[44] Cox, B. T., & Beard, P. C. (2007). The frequency-dependent directivity of a planar Fabry-Perot polymer film ultrasound sensor. IEEE Transactions on Ultrasonics, Ferroelectrics, and Frequency Control, 54(2), 394–404.

[45] Arridge, S. R., Beard, P., Betcke, M. M., Cox, B., Huynh, N., Lucka, F., … Zhang, E. (2016). Accelerated High-Resolution Photoacoustic Tomography via Compressed Sensing. Phys Med Biol, 61, 8908–8940.

[46] Köstli, K. P., Frenz, M., Bebie, H., & Weber, H. P. (2001). Temporal backward projection of optoacoustic pressure transients using Fourier transform methods. Physics in Medicine and Biology, 46(7), 1863–1872.

[47] Caggiati, A., Phillips, M., Lametschwandtner, A., & Allegra, C. (2006). Valves in Small Veins and Venules. European Journal of Vascular and Endovascular Surgery, 32(4), 447–452.

[48] Pu, K., Shuhendler, A. J., Jokerst, J. V., Mei, J., Gambhir, S. S., Bao, Z., & Rao, J. (2014). Semiconducting polymer nanoparticles as photoacoustic molecular imaging probes in living mice. Nature Nanotechnology, 9(3), 233–239.

[49] de Angelis, R., Grassi, W., & Cutolo, M. (2009). A growing need for capillaroscopy in rheumatology. Arthritis & Rheumatism, 61(3), 405–410.

[50] Ingegnoli, F., Boracchi, P., Gualtierotti, R., Lubatti, C., Meani, L., Zahalkova, L., … Fantini, F. (2008). Prognostic model based on nailfold capillaroscopy for identifying Raynaud's phenomenon patients at high risk for the development of a scleroderma spectrum disorder: PRINCE (Prognostic Index for Nailfold Capillaroscopic Examination). Arthritis & Rheumatism, 58(7), 2174–2182.

[51] Allen, T. J., Berendt, M., Lin, D., Alam, S. U., Huynh, N. T., Zhang, E., … Beard, P. C. (2020). High pulse energy fibre laser as an excitation source for photoacoustic tomography. Optics Express, 28(23), 34255.
[52] Hauptmann, A., & Cox, B. (2020). Deep learning in photoacoustic tomography: current approaches and future directions. Journal of Biomedical Optics, 25(11), 1–46. https://doi.org/10.1117/1.JBO.25.11.112903
[53] On Learning the Invisible in Photoacoustic Tomography with Flat Directionally Sensitive Detector, Bolin Pan† and Marta M. Betcke, CurveNet (arxiv.org)
[54] Roustit, M., & Cracowski, J.-L. (2013). Assessment of endothelial and neurovascular function in human skin microcirculation. Trends in Pharmacological Sciences, 34(7), 373–384.
[55] Rossi, M., Matteucci, E., Pesce, M., Consani, C., Franzoni, F., Santoro, G., & Giampietro, O. (2013). Peripheral microvascular dysfunction as an independent predictor of atherosclerotic damage in type 1 diabetes patients: A preliminary study. Clinical Hemorheology and Microcirculation, 54(4), 381–391.
[56] Chao, C. Y. L., & Cheing, G. L. Y. (2009). Microvascular dysfunction in diabetic foot disease and ulceration. Diabetes/Metabolism Research and Reviews, 25(7), 604–614.
[57] Belch JJ, Topol EJ, Agnelli G et al (2003) Critical issues in peripheral arterial disease detection and management: a call to action. Arch Intern Med 163(8):884–892
[58] Han, H.-C. C. (2012). Twisted blood vessels: Symptoms, etiology and biomechanical mechanisms. Journal of Vascular Research, 49(3), 185–197. https://doi.org/10.1159/000335123
[59] Owen, C. G., Newsom, R. S. B., Rudnicka, A. R., Barman, S. A., Woodward, E. G., & Ellis, T. J. (2008). Diabetes and the Tortuosity of Vessels of the Bulbar Conjunctiva. Ophthalmology, 115(6), e27–e32.
[60] Ciurică, S., Lopez-Sublet, M., Loeys, B. L., Radhouani, I., Natarajan, N., Vikkula, M., … Persu, A. (2019). Arterial Tortuosity. Hypertension, 73(5), 951–960.
[61] Almutairi, K. B., Nossent, J. C., Preen, D. B., Keen, H. I., & Inderjeeth, C. A. (2021). The Prevalence of Rheumatoid Arthritis: A Systematic Review of Population-based Studies. The Journal of Rheumatology, 48(5), 669–676.
[62] Wiacek, A., & Lediju Bell, M. A. (2021). Photoacoustic-guided surgery from head to toe [Invited]. Biomedical Optics Express, 12(4), 2079
[63] Ansari, R., Zhang, E. Z., Desjardins, A. E., & Beard, P. C. (2018). All-optical forward-viewing photoacoustic probe for high-resolution 3D endoscopy. Light: Science & Applications, 7(1), 75
[64] Ansari, R., Zhang, E., Desjardins, A., & Beard, P. (2020). Miniature all-optical flexible forward-viewing photoacoustic endoscopy probe for surgical guidance. Optics Letters, 45(22), 6238–6241
[65] Lamont, M., & Beard, P. (2006). 2D imaging of ultrasound fields using CCD array to map output of Fabry-Perot polymer film sensor. Electronics Letters, 42(3), 7–8.
[66] Zhang, E. Z., & Beard, P. C. (2011). A miniature all-optical photoacoustic imaging probe. In A. A. Oraevsky & L. V. Wang (Eds.), Proceedings of SPIE, Photons Plus Ultrasound (Vol. 7899, pp. 78991F-1-78991F – 6). https://doi.org/10.1117/12.874883
[67] Zhang, E. Z., Povazay, B., Laufer, J., Alex, A., Hofer, B., Pedley, B., … Drexler, W. (2011). Multimodal photoacoustic and optical coherence tomography scanner using an all optical detection scheme for 3D morphological skin imaging. Biomedical Optics Express, 2(8), 2202–2215.
[68] Pham, K., Noimark, S., Huynh, N., Zhang, E., Kuklis, F., Jaros, J., … Beard, P. (2021). Broadband All-Optical Plane-Wave Ultrasound Imaging System Based on a Fabry–Perot Scanner. IEEE Transactions on Ultrasonics, Ferroelectrics, and Frequency Control, 68(4), 1007–1016. https://doi.org/10.1109/TUFFC.2020.3028749
[69] H. Yasuda, Plasma Polymerisation (Academic, 1985)
[70] Treeby, B. E., Jaros, J., & Cox, B. T. (2016). Advanced photoacoustic image reconstruction using the k-Wave toolbox. In A. A. Oraevsky & L. V. Wang (Eds.), Proceedings of SPIE (Vol. 9708, p. 97082P).
[71] Treeby, B. E., Varslot, T. K., Zhang, E. Z., Laufer, J. G., & Beard, P. C. (2011). Automatic sound speed selection in photoacoustic image reconstruction using an autofocus approach. Journal of Biomedical Optics, 16(9), 090501.
[72] Köstli, K. P., Frenz, M., Bebie, H., & Weber, H. P. (2001). Temporal backward projection of optoacoustic pressure transients using Fourier transform methods. Physics in Medicine and Biology, 46(7), 1863–1872.
[73] Treeby, B. E., & Cox, B. T. (2010). k-Wave: MATLAB toolbox for the simulation and reconstruction of photoacoustic wave fields. Journal of Biomedical Optics, 15(2), 021314.
[74] BS EN 60825-1:2014+A11:2021 Safety of laser products - Part 1: Equipment classification and requirements